Transition metal doped ceria catalyst prepared by direct precipitation method for thermocatalytic conversion of carbon dioxide via reverse water gas shift

by

Wenxuan Xia

A thesis

presented to the University of Waterloo

in fulfillment of the

thesis requirement for the degree of

Master of Applied Science

in

Chemical Engineering

Waterloo, Ontario, Canada, 2024

© Wenxuan Xia 2024

Author’s declaration

I hereby declare that I am the sole author of this thesis. This is a true copy of the thesis, including any required final revisions, as accepted by my examiners.

I understand that my thesis may be made electronically available to the public.

Abstract

Since the beginning of the industrial revolution, mankind has utilized large amounts of fossil fuels to obtain energy, which has led to the emission of large amounts of greenhouse gases such as carbon dioxide. How to reduce CO_2 and utilize CO_2 to obtain high-value products has become a hot topic in today's research. The thermocatalytic reduction of CO_2 by using renewable H_2 is expected to be a potential solution to these challenges.

In this experiment, the reverse water gas shift (RWGS) reaction of various loaded transition metal doped cerium ($MCeO_2$) catalysts (M = Fe, Co, Ni and Cu) was investigated. The desired catalysts have been synthesized by utilizing the direct precipitation method. The reverse water gas shift reaction has been extensively studied including reaction tests and some characterizations such as X-ray crystallography (XRD), Brunauer Emmett Teller (BET), Temperature Programmed Desorption (TPD), Inductively coupled plasma - optical emission spectrometry (ICP - OES) etc.

In reaction tests, the performance of M-CeO_2 was evaluated in terms of conversion and selectivity by varying the temperature (400°C - 600°C). The resulting reaction products were monitored using an on-line infrared analyzer to identify the formation of carbon monoxide (CO), methane (CH_4), and unconverted CO_2. T-test results show that transition metal doping has a significant effect in enhancing the surface CO_2 adsorption and reduction. effects, including high loading of Fe with higher than 56% CO_2 conversion and 100% selectivity to CO at 600 °C, Cu with 100% selectivity to CO but

lower CO_2 conversion, and Co and Ni with significant methanation ability, especially at high loading.

In addition, the structures of the catalysts before and after the reaction were investigated using XRD. The binding strength of CO_2 on the doped CeO_2 surface was investigated using the programmed temperature rise desorption (TPD) method. The effect of specific surface on CO_2 adsorption was investigated using BET.

This experiment explores the effect of different kinds of transition metal-doped cerium catalysts on the reverse water-gas shift (RWGS) reaction, which reduces excess CO_2 emissions and also provides an idea for CO_2 conversion and utilization.

Acknowledgements

I would like to thank my supervisor Professor David Simakov and Professor Aiping Yu for their continuous support and patient guidance during my program.

I would also like to thank my committee numbers: Professor Rajinder Pal and Professor XiaoYu Wu for their precious comments and suggestions on my project.

This work would not have been possible without the help and advice from my groupmates Kishore Kandasamy, Yue Yu, Yasaman Ghaffarisaeidabad, Zixuan Lin, and Guanjie Sun.

I would also like to acknowledge the support of the Waterloo Institute of Sustainable Energy (WISE), the Ontario Centers of Excellence (OCE), the Canada Foundation for Innovation (CFI), and the Natural Science and Engineering Research Council (NSERC).

Finally, I would like to thank my parents and friends for their support and encouragement throughout my master's program.

Table of Contents

List of figures ixx

Nomenclature xivv

Chapter 1: Background 1

1.1 CO_2 and global emission 1

1.2 Reaction pathways for CO_2 5

1.3 Reverse water gas shift 7

1.4 Project objectives 8

1.5 Thesis outline 9

Chapter 2: Literature review 10

2.1 Noble metal catalyst 10

2.2 Transition metal catalyst 12

2.3 Ceria 14

2.4 Transition metal doped catalyst 16

2.5 Direct precipitation method for catalyst preparation 17

Chapter 3: Methodology 19

3.1 Catalyst synthesis 19

3.2 Experimental techniques 23

3.2.1 X-Ray powder diffraction (XRD) 23

3.2.2 CO_2 Temperature programmed desorption (CO_2 -TPD) 25

3.2.3 Inductively coupled plasma optical emission spectrometry (ICP-OES) 27

3.2.4 Brunauer Emmett Teller (BET) Specific Surface Area (SSA) 29

3.3 Flow system and reaction test 31

3.3.1 Flow system configuration 31

3.3.2 Reactor configuration 32

3.3.3 Reaction test and operating conditions 33

Chapter 4: Catalyst performance and characterization 35

4.1 Structure and composition of fresh and spent catalysts 35

4.2 CO_2 TPD adsorption strength analysis 39

4.3 Catalytic performance evaluation 45

4.3.1 Catalytic performance of Fe-CeO_2 45

4.3.2 Catalytic performance of Co-CeO_2 49

4.3.3 Catalytic performance of Ni-CeO_2 51

4.3.4 Catalytic performance of Cu-CeO_2 52

4.3.5 Comparison of the performance of all catalysts 53

4.4 Correlation between activation energy and desorption energy 54

Chapter 5: Conclusion and future work 56

5.1 Conclusions 56

5.2 Future Work 58

References 61

List of figures

Figure 1. Total U.S. Greenhouse Gas Emissions, 1990-2022[3] 3

Figure 2. Total U.S. Greenhouse Gas Emissions by Economic Sector[3] 4

Figure 3. CO_2 reaction pathways for thermocatalytic hydrogenation[4] 6

Figure 4. Syngas derivatives with reference to their composition(H_2/CO molar ratio)[5] 7

Figure 5. CO_2 conversion to CO during the RWGS reaction over Pt catalysts. (Condition: CO_2 21%, H_2 30%, N_2 balance, total flow rate 100 mL/min^{-1}, 0.5 g catalyst.) [11] 12

Figure 6. the real CO_2 conversion of the CeO_2 and calcined CeO_2 catalysts [17].... 15

Figure 7. DP Synthesis schematic for $MCeO_2$ catalyst preparation 19

Figure 8. Solution preparation procedure for synthesizing $FeCeO_2$ catalyst..... 20

Figure 9. Solution color changes over two hours 21

Figure 10. Picture before and after calcination procedure for synthesizing $FeCeO_2$ catalyst 22

Figure 11. Temperature setting program 22

Figure 12. (left) Bragg's law, (right) schematic of a typical XRD measurement. 24

Figure 13. Schematic picture of CO_2 - TPD 26

Figure 14. Schematic of the ICP-OES instrumentation[36] 28

Figure 15. Schematic diagram of BET theory[37]..... 30

The reactor system (**Figure 16**) which houses the reactor, includes a programmable muffle furnace (KSL-1100X Muffle Furnace, MTI Corporation). A K type thermocouple (1/8″, Omega Engineering) was inserted through the outlet tube so that the thermocouple tip is in contact with the catalyst bed. Feed flow rates were regulated by mass flow controllers (EL-FLOW select mass flow controllers, HOSKIN SCIENTIFIC LIMITED), and pressure was managed by a mechanical back pressure regulator (Stainless Steel BP Regulator, Swagelok). An Agilent Technologies, 5182-9411 silica gel orange column from Fisher Scientific and a mist trap (SMC AFM40-N02-Z-A, SMC Corporation) were used to extract the water. The IR analyzer (IR-208, Infrared Industries, Inc., USA) was used to measure the dry basis concentrations of CO, CO_2, and CH_4 in the outlet stream. LabVIEW (National Instruments) was used to control the entire flow system. Analog-to-digital converters (NI 9215, NI 9263, National Instruments) were used to continuously monitor and record the flow rates, pressure, temperature, and gas concentrations..... 31

Figure 17. Flow system setup for conducting catalytic performance evaluation. Abbreviations: ADC, analog-to-digital converter; BPR, back pressure regulator; RFM, Rotor flow meter; IR, infrared; MFC, mass flow controller; PI, pressure indicator; PC, personal computer; TC, thermocouple; TI, temperature indicator. 32

For reaction tests, a stainless steel (SS) 1/4" tube was used **(Figure 18.)**. Pelletized and sieved catalysts (350-450 µm particle size) were loaded into the reactor through the either side of the SS tube sandwiched by quartz wool on both sides. Post reaction, the catalyst is then removed by removing the quartz wool for post reaction characterization test..... 32

Figure 19. Stainless steel reactor schematic used for reaction tests 33

Figure 20. XRD patterns of fresh a) $FeCeO_2$, b) $CoCeO_2$ catalysts; c) $NiCeO_2$ catalysts, d) $CuCeO_2$ catalysts. 38

Figure 21. XRD pattern of spent a) $FeCeO_2$, b) $CoCeO_2$ catalysts; c) $NiCeO_2$ catalysts, d) $CuCeO_2$ catalysts. 39

Figure 22. CO_2-TPD patterns of fresh a) $FeCeO_2$, b) $CoCeO_2$, c) $NiCeO_2$, d) $CuCeO_2$ catalysts. 40

Figure 23. CO_2-TPD patterns and the deconvoluted adsorption peaks of fresh metal doped CeO_2 catalysts 42

Figure 24. Activation energy of desorption of weak, medium and strong adsorbed CO_2 on metal doped CeO_2 surfaces calculated from CO_2-TPD 43

Figure 25. a) CO_2 conversion as a function of temperature (400-600°C) a) $FeCeO_2$, b) $CoCeO_2$, c) $NiCeO_2$, d) $CuCeO_2$ catalysts. Condition: GHSV = 60,000 mL $h^{-1}gcat^{-1}$, H_2/CO_2 = 3:1, P = 3 bar (absolute). The solid black line represents the

of RWGS. Red diamond, yellow triangle and green square represent the high, medium and loading $MCeO_2$ catalysts respectively. 46

Figure 26. Selectivity towards CO as a function of temperature of a) $FeCeO_2$, b) $CoCeO_2$, c) $NiCeO_2$, d) $CuCeO_2$ catalysts. Condition: GHSV = 60,000 mL $h^{-1}gcat^{-1}$, H_2/CO_2 = 3:1, P = 3 bar (absolute). Red diamond, yellow triangle and green square represent the high, medium and loading $MCeO_2$ catalysts respectively. 47

Arrhenius plots for pure CeO_2 and $FeCeO_2$ catalysts shown in **Figure 27a** was obtained by a separate set of reactions tests. CO generation rates were calculated from **Eq. (21)** and activation energy estimation was done using **Eq. (22).** 48

Figure 28.Selectivity towards CO as a function of temperature of a) $FeCeO_2$, b) $CoCeO_2$, c) $NiCeO_2$, d) $CuCeO_2$ catalysts. Condition: GHSV = 60,000 mL $h^{-1}gcat^{-1}$, H_2/CO_2 = 3:1, P = 3 bar (absolute). Red diamond, yellow triangle and green square represent the high, medium and loading $MCeO_2$ catalysts respectively. 49

Figure 29. a) $E_{a,rxn}$ as a function of transition metal loading and star represents pure CeO_2; b) Experimental activation energy ($E_{a,rxn}$) for different mMCe catalysts 54

Figure 30. Activation energy measured from performance tests ($E_{a,rxn}$) as a function of activation energy of CO_2 desorption from the medium strength site ($E_{a,des}$). Star represents pure CeO_2. 55

Nomenclature

A	pre-exponential factor, mol/(s kg)
A_s	area occupied by a single surface atom, nm^2/CeO_2
D	dispersion of catalyst
d(SSA)	SSA-based particle size, nm
d(XRD)	XRD-based particle size, nm
E_a	activation energy, kJ/mol
$E_{a,des}$	activation energy of desorption, kJ/mol
$E_{a,rxn}$	activation energy of reaction, kJ/mol
F_i	input flow rate (i stands for either CO_2, CO, or CH_4), mol/s
f_1	CO_2 conversion to CO
f_2	CO_2 conversion to CH_4
ΔH°_{298}	reaction enthalpy, kJ/mol
K	Scherrer equation shape factor
M_W	molar mass of CeO_2, g/mol
N_a	Avogadro's number
P	pressure, bar
R_g	gas constant, $\mathrm{J/(K\ mol)}$
R	CO_2 conversion rate, mmol/(g s)
R_{CO}	CO generation rate, mol/(s kg)
S_{CO}	CO selectivity
s	adsorption cross-sectional area of the adsorbed species
T	temperature, °C (K in Arrhenius equation)
T_{max}	peak temperature from TPD, °C
X_{CO_2}	CO_2 conversion
x	weight fraction, wt%
y_i	mole fraction (i stands for either CO_2, CO, or CH_4)

Greek letters

α	H_2:CO_2 ratio in the feed
B	full width at half maximum, radian
θ	diffraction angle, °
λ	X-ray wavelength, nm
v_1	frequency factor, s^{-1}

Abbreviations

BET	Brunauer–Emmett–Teller
CB	carbon balance
DP	direct precipitation
FTIR	Fourier transform infrared spectroscopy
GHGs	greenhouse gas
GHSV	gas hourly space velocity
ICP-OES	inductively coupled plasma optical emission spectroscopy
IR	infrared
RWGS	reverse water gas shift
SSA	specific surface area
TGA	thermo-gravimetric analysis
TPD	temperature programmed desorption
WGS	water gas shift
XRD	X-ray diffraction

Chapter 1: Background

1.1 CO_2 and global emission

Since mankind entered the industrial revolution, human society has begun to enjoy the benefits of industrialization. At the same time, however, the demand for energy has increased. Currently, humans utilize a large amount of fossil fuels to obtain energy, which has led to the emission of large amounts of greenhouse gases (GHGs). Carbon dioxide, a common greenhouse gas and acidic gas, contributes to the greenhouse effect and the acidification of seawater, which in turn leads to climate extremes and a sharp decline in biodiversity. According to the International Energy Agency, global energy-related CO_2 emissions grew by 1.1% in 2023, increasing 410 million tons (Mt) to reach a new record high of 37.4 billion tones (Gt). This compares with an increase of 490 Mt in 2022 (1.3%). Emissions from coal accounted for more than 65% of the increase in 2023[1]. Global CO_2 emissions for 2022 increased by 1.5% relative to 2021 (+7.9% and +2.0% relative to 2020 and 2019, respectively), reaching 36.1 Gt CO_2. These 2022 emissions consumed 13%–36% of the remaining carbon budget to limit warming to 1.5 °C, suggesting permissible emissions could be depleted within 2–7 years[2]. Climate extremes caused by excessive CO_2 emissions can lead to further increases in energy demand and CO_2 emissions. Since large amounts of CO_2 emissions have a huge impact on the survival of the human race, it is

crucial to identify the causes of excessive CO_2 emissions and to find the most appropriate solutions.

According to United States Environmental Protection Agency **(Figure 1)**, in 2022, U.S. greenhouse gas emissions increased 0.2% compared to 2021 levels. In 2020, there was a sharp decline in emissions largely due to the impacts of the coronavirus (COVID-19) pandemic on travel and other economic activity. In 2021 and 2022, the increase in total greenhouse gas emissions was driven largely by an increase in CO_2 emissions from fossil fuel combustion due to the continued rebound in economic activity after the height of the COVID-19 pandemic. In 2022, CO_2 emissions from fossil fuel combustion increased by 8% relative to 2020 and 1% relative to 2021[3].

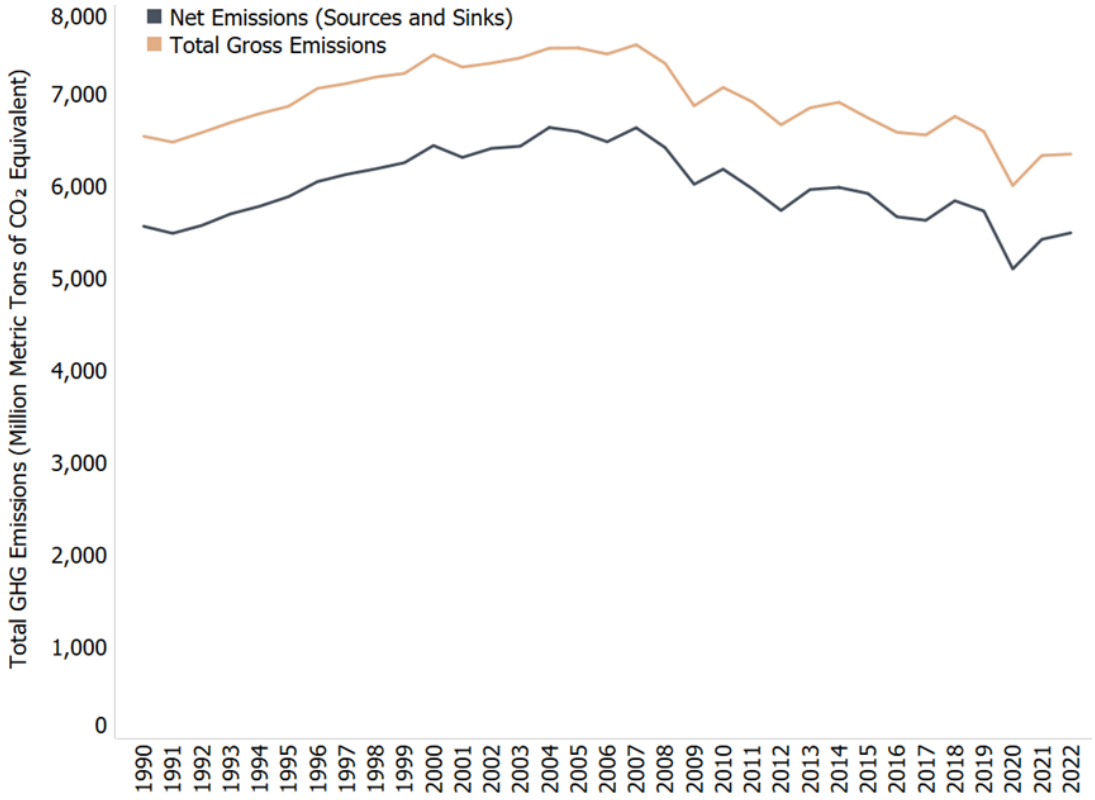


Figure 1. Total U.S. Greenhouse Gas Emissions, 1990-2022[3]

In the United States, for example, these greenhouse gases come from these five main sources, transportation, electric power, industry, commercial and residential and agriculture. The United States emits 6,343.2 million metric tons of carbon dioxide in the year 2022, and this emissions in the United States in 2022 will be 6,343.2 million metric tons of carbon dioxide, and this CO_2 will come primarily from transportation, which will account for 28% of the total, followed by electric power, which will account for 25% of the total.

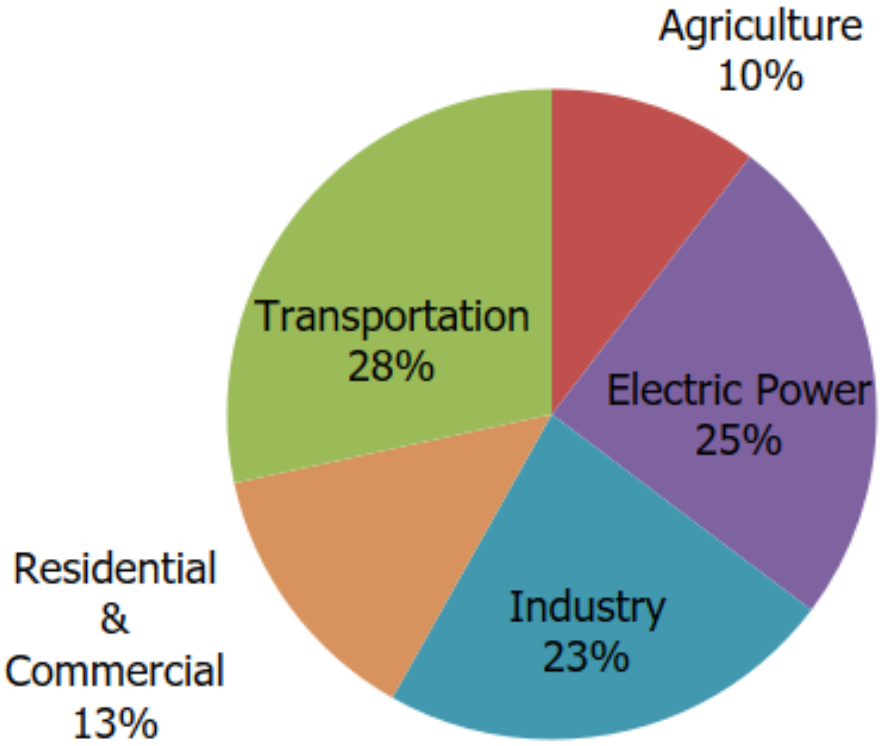


Figure 2. Total U.S. Greenhouse Gas Emissions by Economic Sector[3]

All of the above information indicates that, in such a serious situation, it is urgent to find a solution to the problem of excessive CO_2 emissions. Currently, the synthesis of high-value chemical products using CO_2 is one of the solutions to the problem of excessive CO_2 emissions. This approach not only reduces the burning of fossil fuels, but also establishes a new energy supply chain and supply model, increasing the diversity of energy supply.

1.2 Reaction pathways for CO_2

Carbon dioxide capture and storage (CCS) and carbon dioxide capture and utilization (CCU) are promising application for reducing carbon dioxide emissions. Carbon dioxide capture and storage (CCS) is a promising solution to the carbon dioxide problem because it allows for the direct separation of carbon dioxide from the outlet stream and its transportation to the subsurface. Various processes have been investigated for separating CO_2 from the outlet stream, including amine scrubbing and membrane separation methods. However, the long-term impacts of storing carbon in groundwater reservoirs are unknown. In contrast, CCUs are of interest because they can convert emitted CO_2 into useful products such as synthetic fuels. The ability to create artificial carbon cycles and convert CO_2 emissions into profitable resources has accelerated research in this area.

Although there are many different reaction pathways for CO_2, such as electrochemical, photochemical and biological methods. These methods have limitations, for example, electrochemical reduction and photochemical reduction have their own capacity and limitation of efficiency. Thermal catalysis, as a very mature reaction pathway, has more advantages than the above reaction pathways, such as mature technology, easy manipulation, and the ability to combine high temperature and catalytic reaction to increase CO_2 conversion.

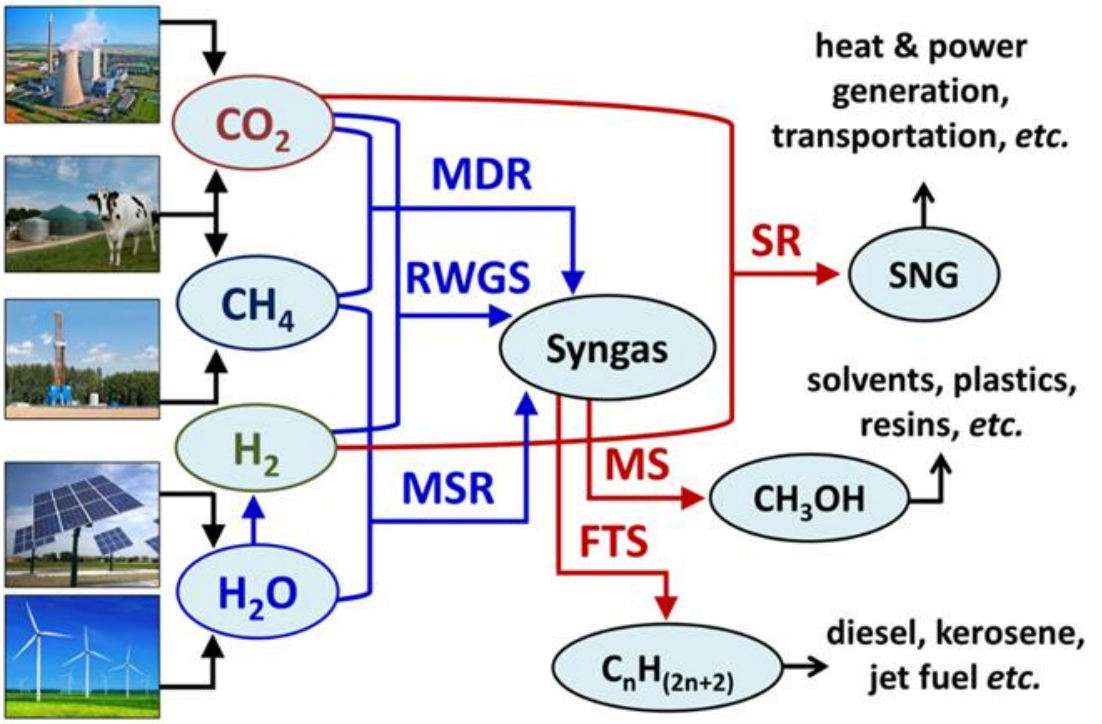


Figure 3. CO_2 reaction pathways for thermocatalytic hydrogenation[4]

This **Figure. 3.** shows pictures of the various conversion pathways to get syngas. There are three ways to obtain syngas, and they are reverse water gas shift reaction (RWGS), methane dry reforming (MDR) and process of methane steam reforming (MSR). In the MSR reaction, water and CO_2 react to produce syngas with CO and H_2 as the main components. Syngas can also be generated by MDR using CO_2 and CH_4. Syngas can also be obtained by the RWGS method using H_2 and CO_2.

Syngas is a mixture of gases that usually consist of CO and H_2 but may also contain some other gaseous components such as CO_2 and CH_4. Syngas has a wide range of uses and the pictures show some of the main uses of syngas[5], show in

Figure 4. By utilizing syngas, CO_2 can be converted into high-value chemical products, while at the same time solving the problem of excessive CO_2 emissions.

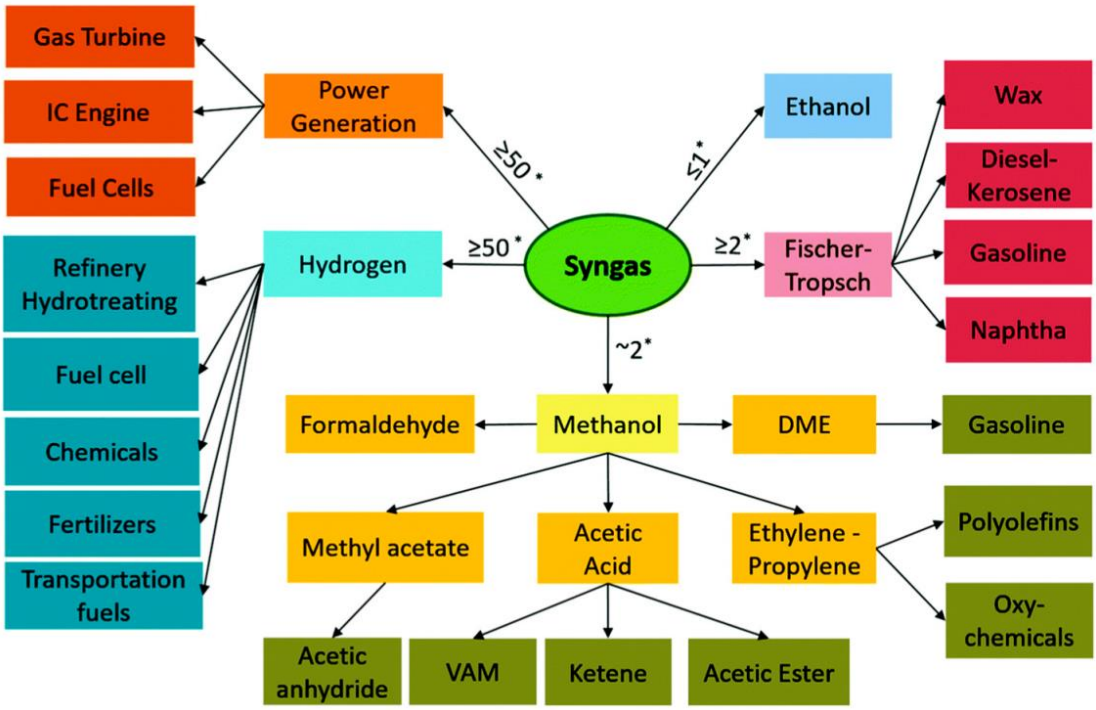


Figure 4. Syngas derivatives with reference to their composition(H_2/CO molar ratio)[5]

1.3 Reverse water gas shift

Obtaining syngas through the RWGS reaction is a crucial step in realizing the conversion of CO_2 into high-value chemical feedstocks. During the RWGS reaction **(Equation (1))** utilizing CO_2 and H_2, Sabatier reaction **(Equation (2))** and CO methanation **(Equation (3))** occur simultaneously as side reactions, both of which lead to the formation of CH_4.

$$CO_2 + H_2 \rightarrow CO + H_2O \qquad \Delta H^{\circ}_{298} = +41.2\ \text{kJ/mol} \tag{1}$$

$$CO_2 + 4H_2 \rightarrow CH_4 + 2H_2O \quad \Delta H^{\circ}_{298} = -164.9\ \text{kJ/mol} \tag{2}$$

$$CO + 3H_2 \rightarrow CH_4 + H_2O \quad \Delta H^{\circ}_{298} = -206.5\ \text{kJ/mol} \tag{3}$$

RWGS, as a heat-absorbing reaction, should be reacted at high temperatures, given an appropriate H_2:CO_2 feed ratio and a suitable catalyst. These conditions provide flexibility in the output products that can be produced by RWGS[6]. At the same time the H_2O generated by the reaction should be promptly removed from the water by using a desiccant bed or a membrane which is permeable to water.

However, at higher temperatures, the catalyst suffers from reduced activity due to coking and sintering[7]. Therefore, in order to achieve high CO_2 conversion and high CO selectivity, there is therefore an urgent need to develop catalysts with high activity at lower temperatures (<600°C) and selectivity for CO.

1.4 Project objectives

Main goal:

The main objective of this thesis is to develop and evaluate transition metal doped cerium (M-CeO_2) catalysts (M = Fe, Co, Ni and Cu) to achieve high activity for the reverse water gas shift reaction (RWGS) and high selectivity for carbon monoxide (CO). The comprehensive characterization of the catalysts using multiple analytical techniques is designed to provide a detailed description of the structural, chemical and physical properties, which will provide insight into the catalysts' properties and

enhance the activity of the RWGS reaction. Here are the specific objectives for this project: Evaluation of transition metal doped ceria catalyst synthesized via direct precipitation method (DP) and evaluate the structure-activity relationship of the catalyst for the RWGS reaction.

1.5 Thesis outline

Chapter 2 summarizes literature review for RWGS catalyst which includes noble metal, transition metal and metal oxides catalyst.

Chapter 3 shows the synthesis method used for this project. Chapter 3 also gives the characterization method used in this project to evaluate all the catalysts. This includes a brief schematic and explanation of characterization techniques like X-Ray diffraction (XRD), Brunauer–Emmett–Teller (BET) and temperature programmed desorption. Additionally, a detailed schematic of the flow system utilized for the reaction test is also provided.

Chapter 4 presents the results of the transition metal doped ceria evaluated for RWGS. It includes both characterization and reaction test results for this project and some discussion on the structure of an activity relationship.

Finally, chapter 5 briefly concludes the results presented and provides some insights on how this work can be improved.

Chapter 2: Literature review

2.1 Noble metal catalyst

Noble metals are often used in catalysis because of their excellent properties. Noble metal catalysts like Rh, Ru, Pt and Pd are widely used in RWGS reactions[8]. The incomplete d-orbital combined with oxidation properties of noble metals resulted in excellent performance for RWGS reaction and promising corrosion resistant properties as well. Lebarbier et al.[9] test the catalytic activity of Pd/ZnO catalysts for the reverse water gas shift reaction was tested at 250-400 ℃, at feed ratio of N_2:H_2:CO_2 = 6:1:1, using a fixed-bed quartz tube reactor. The results showed that CO_2 conversion decreased with increasing reduction temperature. The PdZn particle size was found to increase with increasing Pd loading and reduction temperature by XRD. Increasing the reduction in temperature leads to a sintering effect and consequently to an increase in PdZn particle size. Thus, the PdZn catalysts are structurally sensitive to the reverse water gas shift reaction. The rate of CO formation or CO_2 conversion increases with decreasing PdZn particle size. Kwak et al.[10] prepared atomically dispersed Pd/Al_2O_3 which can catalyze CO_2 into CO efficiently. At low Ru loadings (⩽0.5%), the active metal phase is highly dispersed (mostly in atomic form) on the alumina carrier and CO is formed with high selectivity. As the metal loading increases, the selectivity of CH_4 formation increases while the selectivity of CO generation decreases.

Kim et al.[11] prepared Pt/TiO_2 and Pt/Al_2O_3 catalysts and investigated the effect of the reducing properties of the carriers on the reaction mechanism of the reverse water gas shift using a fixed-bed reactor. As shown in **Fig. 5.** The Pt/TiO_2 catalyst performed better than the Pt/Al_2O_3 catalyst at all temperatures tested. In addition, it was very close to equilibrium at reaction temperatures of 673 K or higher. It was found that the inverse water gas shift reaction proceeds through a redox mechanism between the Pt sites on the catalyst surface and the sites of the reducible carriers, with the formation of Pt-O v -Ti^{3+} sites in the Pt/TiO_2 catalysts due to the reducible nature of the TiO_2 carriers. This leads to a strong electron-donating property, which is typical of the SMSI effect.

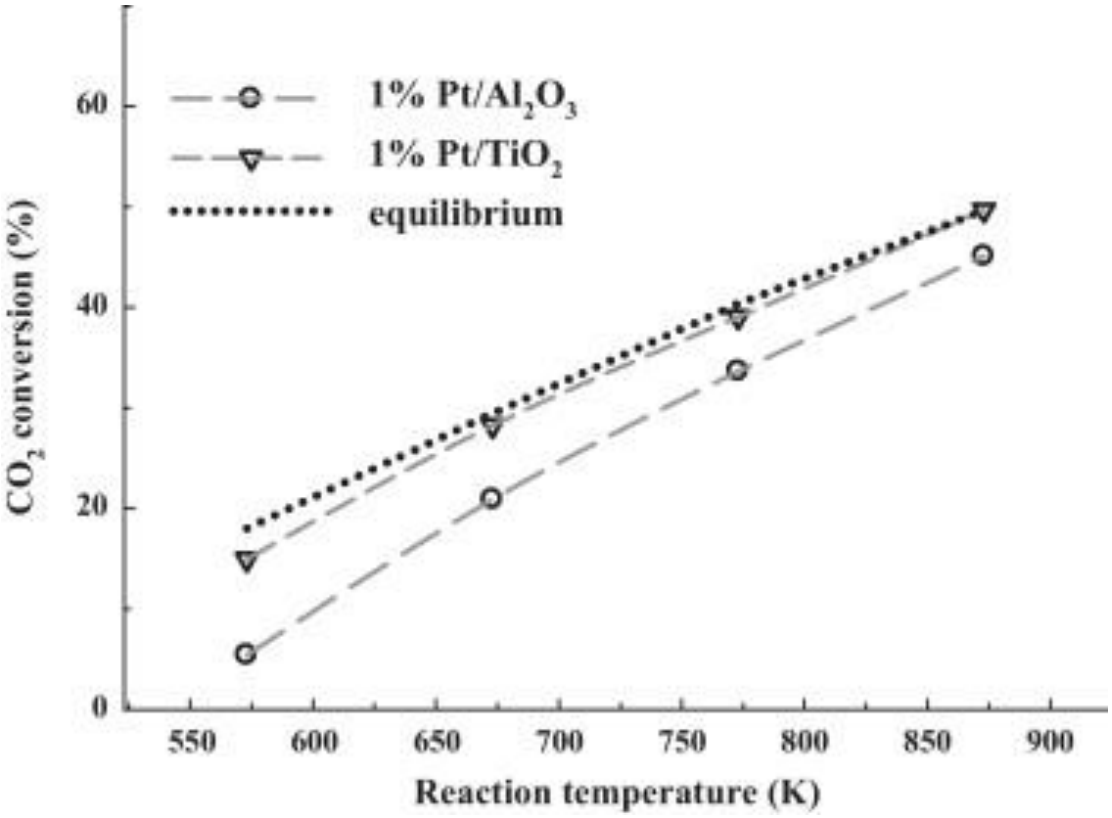


Figure 5. CO_2 conversion to CO during the RWGS reaction over Pt catalysts. (Condition: CO_2 21%, H_2 30%, N_2 balance, total flow rate 100 mL/min^{-1}, 0.5 g catalyst.) [11]

Although noble metals show very good performance as catalysts for RWGS reactions, expensive prices and high methane conversion rates have led to noble metals becoming impractical as catalysts in industry.

2.2 Transition metal catalyst

Because of their high activity in hydrogenation reactions like the water gas shift reaction and their affordability, transition metal catalysts like Fe, Co, Ni, and Cu have attracted a lot of attention. The catalysts Fe/γ-Al_2O_3 and Fe-K/γ-Al_2O_3 were produced by Loiland et al.[12] using a packed-bed reactor, the only tiny byproduct was methane

(CH_4), and the selectivity for CO was continuously higher than 99% for all materials at equal moles of CO_2 and H_2. The rate of CO production is significantly increased by doping potassium into Fe/Al_2O_3. Excess CO_2 slowly deactivates Fe/Al_2O_3 and $Fe-K/Al_2O_3$, although excess H_2 results in steady catalytic rates. The reaction rate's stronger reliance on H_2 as opposed to CO_2.

Zakharova and colleagues[13] synthesized a High-Surface-Area $Cu/\gamma-Al_2O_3$ catalyst by Reverse microemulsion method that exhibited full CO selectivity and 40% conversion at 500 °C, P = 3 bar, $H_2:CO_2$ = 4:1, and GHSV = 10,000 mL/(gh). At 500–600 °C, the catalyst achieves almost equilibrium CO_2 conversion and is completely selective for CO production. The catalyst was shown to be totally selective for CO and comparatively stable based on stability experiments conducted at various wind speeds.

Sun et al.[14] get Ni/Ce–Zr–O catalyst were synthesized via impregnation and applied in the reverse water gas shift reaction. For Ni/Ce–Zr–O, the reaction temperature at the range of 550 °C to 750 °C was examined at 1 atm and a total flow rate of 50 ml/min with an $H_2:CO_2$ ratio of 1:1. As temperature rises, CO_2 conversion increases across the board for all catalysts, suggesting that high temperatures are advantageous for CO_2 conversion. The best selectivity for CO is 99.65% at 750 °C and the selectivity of CH_4 decreases with temperature, and at 700°C, none CH_4 is formed, which suggesting that CH_4 production can be suppressed at high temperatures.

2.3 Ceria

Because of its remarkable reversible reducibility and widespread application as a support material, cerium (CeO_2) has been the subject of increased research[15]. CeO_2 can store and release oxygen reversibly, changing its chemical state from Ce^{4+} to Ce^{3+} (by the creation of oxygen vacancies)[16].

CeO_2 nanorods were synthesized via a hydrothermal method and using thermal calcination under air atmosphere at 200, 300, 500 and 600°C[17]. At atmospheric pressure, the hydrogenation of CO_2 was assessed in a fixed bed quartz reactor. After CeO_2 catalyst was put into the reactor bed, 200 mg of catalyst was pretreated in Ar (30 $mL \cdot min^{-1}$) at 300 °C for 30 minutes. After then, cool down the catalyst to room temperature. Subsequently, the reactor was filled with a mixed gas consisting of CO_2 (2 $mL \cdot min^{-1}$), H_2 (6 $mL \cdot min^{-1}$), and Ar (42 $mL \cdot min^{-1}$), which achieved a steady state in one hour. **Figure. 6.** showing the CO_2 conversion of the catalyst at different temperatures. Direct evidence is that CO_2 hydrogenation on CeO_2 favors a redox process with the cycle of formation and annihilation of oxygen vacancies is provided by in-situ DRIFTS and isotope steady-state studies. The optimal catalytic activity is produced by medium surface levels of structural flaws, which maintain a balance between H_2 activation and CO_2 dissociation.

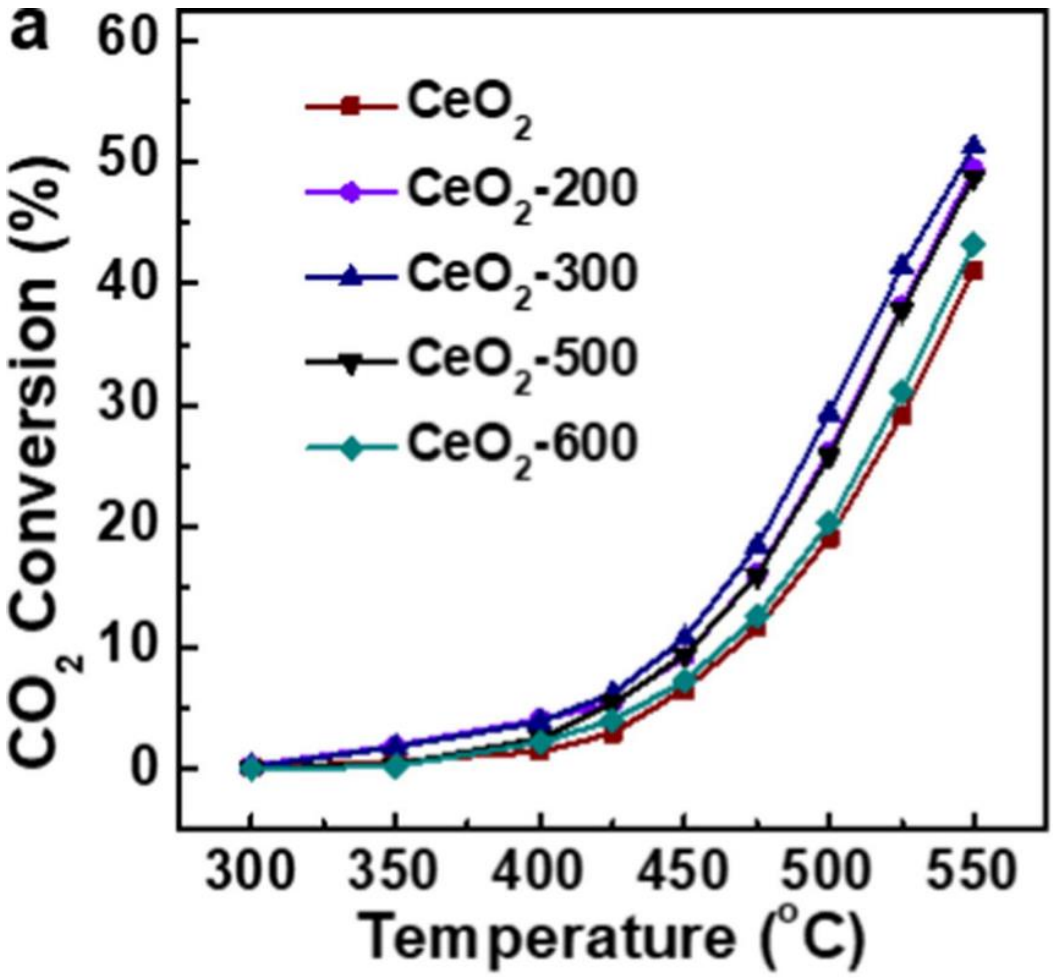


Figure 6. the real CO_2 conversion of the CeO_2 and calcined CeO_2 catalysts [17]

CeO_2 synthesized via hard template, complex and precipitation methods were investigated by Dai et al.[18]. The reaction tests were carried out at atmospheric pressure within the temperature range of 300-580 °C. The feed ratio of H_2 to CO_2 was set at 4, and the gas hourly space velocity (GHSV) was maintained at 60,000 mL/ (g h). The results revealed that all catalysts show 100% selectivity towards CO, with conversion rates ranging from 9% to 16% at a temperature of 580 °C.

2.4 Transition metal doped catalyst

While cerium oxide (CeO_2) has shown considerable selectivity towards the reverse water gas shift (RWGS) reaction, reported levels of CO_2 conversion frequently do not reach equilibrium values. Achieving equilibrium in CO_2 conversion remains a challenge despite CeO_2's noted selectivity towards RWGS. In broad terms, CeO_2 is considered a subpar catalyst, with its ability to generate oxygen vacancies being limited[19]. Numerous investigations have indicated that the incorporation of transition metals into CeO_2 can markedly enhance catalytic activity for the desired reaction pathway[20]. Specifically, nickel, cobalt, copper, and iron can be easily integrated into the CeO_2 lattice to induce the formation of oxygen vacancies. Additionally, CeO_2 can serve as a supportive material in such configurations. For example, Oxygen vacancies were formed in CeO_2 lattice due to the incorporation of Ni^{2+} ions into ceria lattice. Oxygen vacancies formed in ceria lattice and highly dispersed Ni were key active components for RWGS, and bulk Ni was key active component for methanation of CO_2[21]. Sun et al.[22] prepared yttrium-modified Ni/CeO_2 catalysts, revealing that methane is the primary product for Ni-based catalysts. Yang et al.got Fe/CeO_2-Al_2O_3 catalysts for RWGS[23]. Fe-based catalysts supported on CeO_2-Al_2O_3 effectively catalyze the reverse water-gas shift reaction. Addition of promoters like Ni and Cu significantly enhances CO_2 conversion capacity due to strong interactions between Fe and Ni/Cu, altering Fe's electronic density and

facilitating CO_2 activation on the catalytic surface, as confirmed by XPS. Ni and Cu act not only as dopants but also as co-catalysts, contributing to the reaction's intrinsic activity.

2.5 Direct precipitation method for catalyst preparation

Direct precipitation, also known as chemical precipitation, refers to the transformation of a liquid into a solid by either converting the liquid into an insoluble form or saturating the solution beyond its capacity. Precipitation reaction is a chemical process that takes place in a water-based solution when two ionic compounds react, resulting in the formation of an insoluble salt called precipitates.

The direct precipitation method is widely used due to its simplicity and economical cost. Current synthetic methods include thermal decomposition[24], chemical vapor deposition[25], sol-gel[26], spray pyrolysis[27], and precipitation[28], but among these synthetic routes, precipitation provides an easy way for low-cost, large-scale production without the need for costly raw materials and complex equipment compared to other traditional methods[29]. Using this method, large quantities can be prepared in a short period of time, which is conducive to industrialization.

The direct precipitation technique involves the following steps: a measured amount of solution containing a soluble salt is poured in a beaker, then solutions of additional soluble salts are added and mixed until no more solid forms. The precipitate is then

filtered out and the residue is the insoluble salt obtained. The residue is finally washed with a solvent.

Chapter 3: Methodology

3.1 Catalyst synthesis

CeO_2 can accommodate the substitution of Ce in its lattice by lanthanides, transition metals, and noble metals. This substitution can lead to the formation of defects and affect the migration ability of lattice oxygen within the CeO_2 structure. Transition metal M (M=Fe, Ni, Co and Cu) has the ability to substitute Ce in CeO_2 lattice

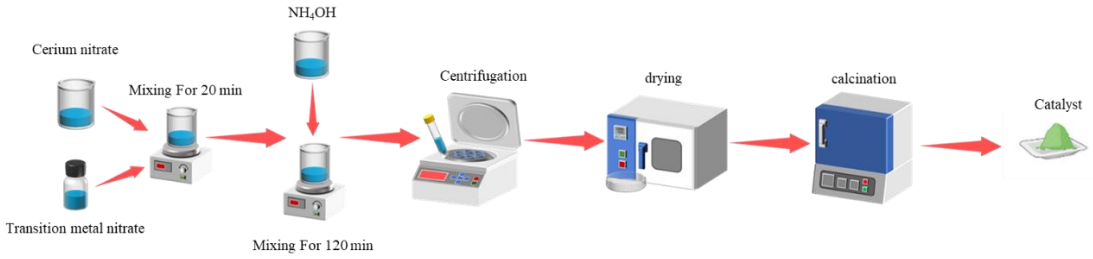


Figure 7. DP Synthesis schematic for $MCeO_2$ catalyst preparation

The following steps were carried out for the synthesis of $FeCeO_2$ catalyst. Three different solutions were prepared for this catalyst. In this experiment, deionized water was used to prepare 0.29 M solutions of cerium nitrate (99.5% Ce $(NO_3)_3 \cdot 6H_2O$, Alfa Aesar) and iron nitrate (Fe $(NO_3)_3 \cdot 9H_2O$, Sigma-Aldrich) separately. First, the appropriate amounts of cerium nitrate and the iron nitrate were accurately weighed and dissolved in deionized water to ensure concentrations. Next, these two solutions were combined in a predetermined ratio. The resulting mixture was then placed on a magnetic stirrer and stirred at room temperature (20 °C) for 20 minutes at an

appropriate speed to ensure thorough mixing. After thorough stirring, the pH of the solution was measured using a pH meter. Ammonium hydroxide (28-30% NH_4OH, LabChem Inc.) was then added to the solution until the pH reached 11. Subsequently, the stirring speed was increased to ensure that the reaction proceeded fully. The solution was maintained under these conditions for 2 hours to ensure complete reaction. The color changes over two hours are shown in the graph.

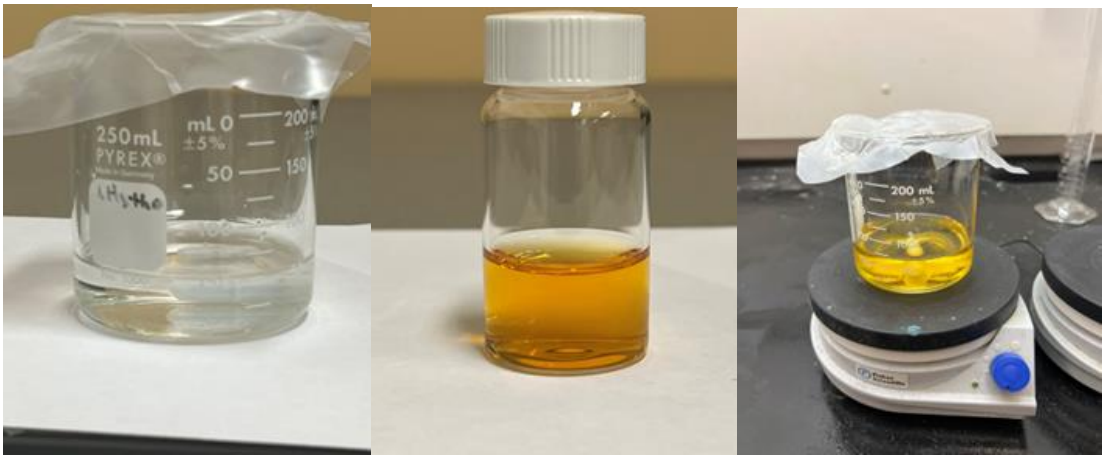


Figure 8. Solution preparation procedure for synthesizing $FeCeO_2$ catalyst

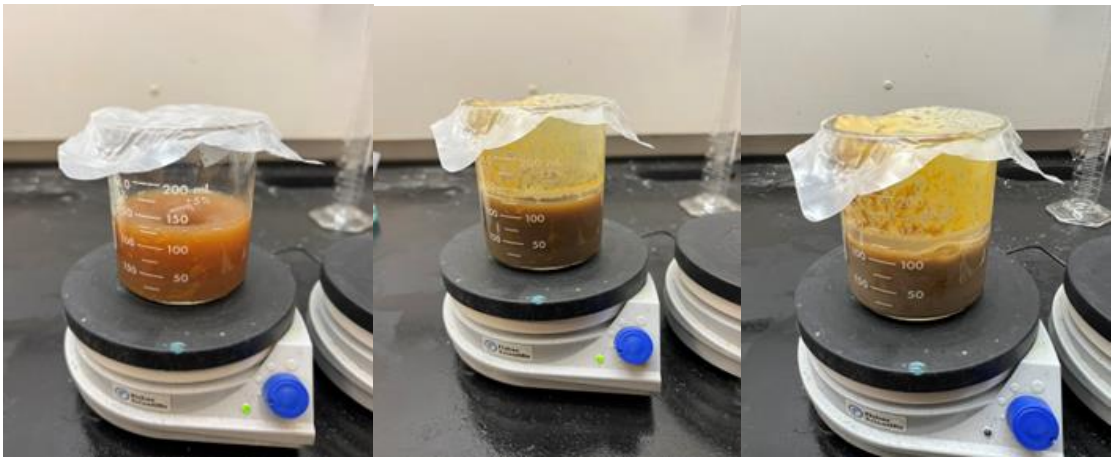


Figure 9. Solution color changes over two hours

Following that, centrifugation was performed at 3500 rpm for 10 minutes by using a centrifuge. The pH of the solution was assessed by using pH strips and the precipitate was washed with deionized water. This centrifugation and washing process was repeated until the pH reached 8.

The precipitate was placed in a drying oven overnight at 120 °C. After drying, the sample was ground into a powder and evenly spread in a calcination boat. Using a muffle furnace, the calcination process was conducted according to the temperature profile shown in the diagram. The furnace temperature was set to ramp up from room temperature to 400 °C within 30 minutes and hold at 400 °C for 240 minutes. After that, the temperature was lowered to room temperature over 30 minutes.



Figure 10. Picture before and after calcination procedure for synthesizing $FeCeO_2$ catalyst

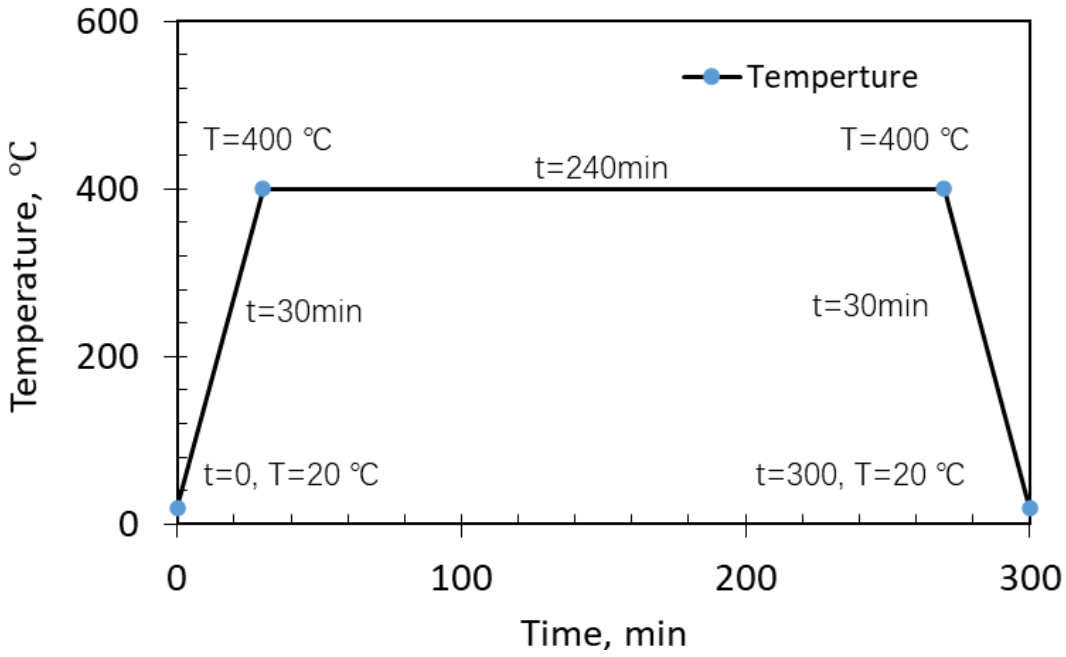


Figure 11. Temperature setting program

A similar procedure was done for $NiCeO_2$, $CoCeO_2$ and $CuCeO_2$ as well. Each $MCeO_2$(M=Fe, Ni, Co and Cu) have three different loading (high, medium, and low

load). Pure CeO_2 and twelve CeO_2 catalysts were synthesized using the direct precipitation (DP) method.

3.2 Experimental techniques

In this section, all analytical techniques used in this study are briefly presented with its fundamental principles and schematics (if applicable). These methods are used to evaluate the catalyst composition, morphology and performance.

3.2.1 X-Ray powder diffraction (XRD)

XRD is a widely used analytical technique in materials science and chemistry to determine crystallite size, crystallite structure, and the catalyst's theoretical density. [30]. The principle of XRD is based on Bragg's law. This law states that when incident X-rays interfere with the lattice planes of a crystal, the constructive interference results in the diffraction of X-rays. The mathematical expression for Bragg's law is: $n\lambda = 2d\sin\theta$, (n=1, 2, 3...) where λ, d, θ represent the wavelength of the X-rays, the crystal lattice plane spacing, and the angle between the incident X-rays and the corresponding crystal plane, respectively.

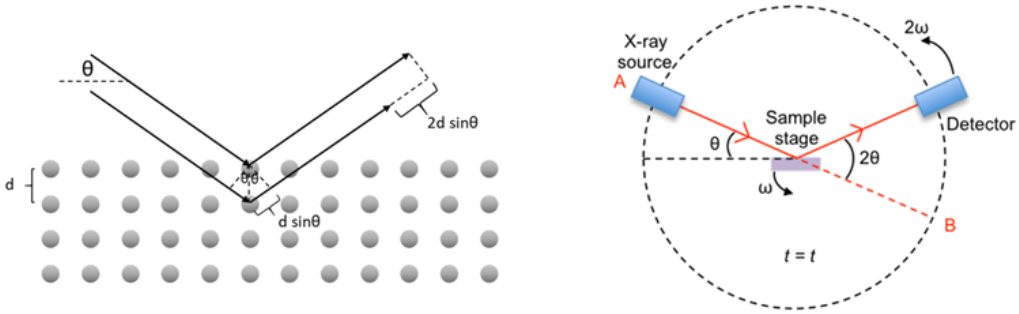


Figure 12. (left) Bragg's law, (right) schematic of a typical XRD measurement[30].

The **figure 12** illustrates that the difference in optical range between two adjacent crystal surfaces illuminated by X-rays is 2dsinθ when X-rays are irradiated into a crystal[31]. The diffracted intensities of the X-rays will be enhanced by one another if the difference in optical range is equal to n times the wavelength of the X-rays; on the other hand, the diffracted intensities elsewhere will remain unchanged or weaken.

In an XRD experiment, X-rays are produced by an X-ray tube and directed towards a sample. A diffraction pattern is created when the sample's lattice planes diffract. By adjusting the angle of incidence and the position of the detector, the intensity and position of the different diffraction levels can be measured. Experimentally obtained XRD patterns usually have intensity as the vertical axis and 2θ (double the angle of incidence) as the horizontal axis. Each diffraction peak corresponds to diffraction

from a different lattice plane in the crystal. By analyzing the position and intensity of these peaks, structural information about the crystal can be inferred.

Bruker EVA software was used to analyze the X-ray diffraction (XRD) patterns that were obtained using Rigaku MiniFlex II. The Scherrer equation[32], Equation (4), was used to calculate the crystallite size using the Bruker EVA software.

$$D_{XRD} = \frac{K\lambda}{\beta \cos\theta} \tag{4}$$

3.2.2 CO_2 Temperature programmed desorption (CO_2 -TPD)

TPD stands for Thermal Desorption Program and is an experimental technique used to study the adsorption and desorption processes on material surfaces. Desorption happens when heat is applied to a solid material to the point where molecules adsorbed on the surface can cross the energy barriers that prevent them from escaping (also known as the activation energy for desorption). The binding capacity between different adsorbates and the same surface, or between the same adsorbate and adsorption centers with different properties on the surface, requires different energies for desorption. Therefore, the results of thermal desorption experiments reflect not only the binding capacity of the adsorbent to the solid surface, but it also reflects the kinetic behavior at the temperature and surface coverage at which the desorption occurs[33].

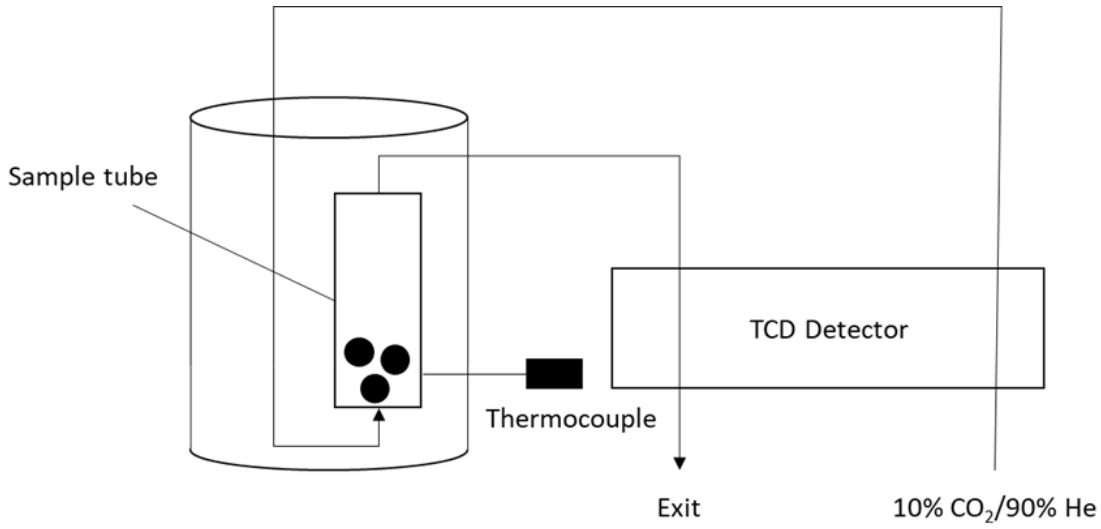


Figure 13. Schematic picture of CO_2 - TPD

Figure 13. shows a schematic picture of CO_2 - TPD. The TPD profiles can be analyzed to answer the number of adsorbed species and their approximate concentration based on the number of peaks on the TPD curves, the location of the peaks, and the size of the peak areas. The activation energy of desorption for each species can be determined using different initial coverage or heating rates, allowing the strength of species binding to the surface to be evaluated. The number of reaction levels and species morphology can be determined using desorption kinetics in conjunction with other methods such as infrared absorption spectroscopy, nuclear magnetic resonance, mass spectrometry, and so on.

Equation 5 was used to determine the activation energy of desorption. By using the Polanyi-Wigner equation where T_{max} is peak temperature from TPD, β is the TPD heating rate, R is the gas constant and v_1 is the frequency factor. According to the

Redhead analysis hypothesis, the activation parameters are considered to be independent of surface coverage, meaning that they do not vary with changes in the amount of adsorbate on the surface. Additionally, the desorption process is assumed to follow first-order kinetics, implying that the rate of desorption is directly proportional to the concentration of the adsorbed species. These assumptions simplify the analysis and allow for a more straightforward interpretation of the desorption data obtained from Temperature Programmed Desorption experiments[34].

$$\Delta E_{des} = RT_{\max}\left[\ln\frac{\nu_1 \cdot T_{\max}}{\beta} - \ln\frac{\Delta E_{des}}{RT_{\max}}\right] \quad (5)$$

3.2.3 Inductively coupled plasma optical emission spectrometry (ICP-OES)

The Inductively coupled plasma-optical emission spectrometer, or ICP-OES, is a tool used to analyze analytical samples qualitatively and quantitatively for up to 70 metallic elements and a few non-metallic elements. The domains of geology, ecology, biology, medicine, metallurgy, agriculture, food science, and chemical industry all make extensive use of it[35].

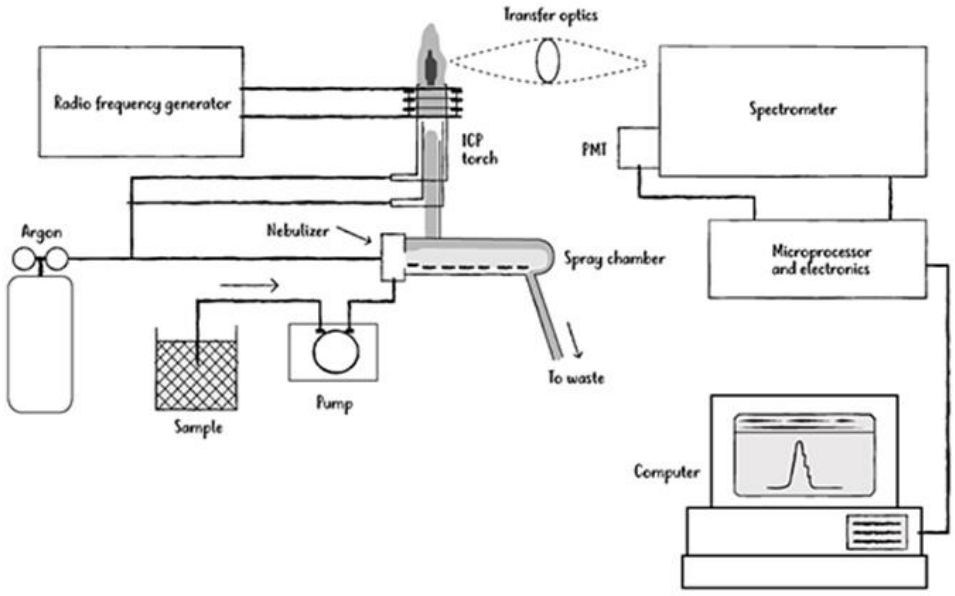


Figure 14. Schematic of the ICP-OES instrumentation[36]

Figure 14. shows a schematic of ICP-OES. Excitation, spectral analysis, and detection are the three primary processes in the ICP-OES operating principle. An element in the sample is evaporated, vaporized, or dissociated into an atomic state through the use of an inductively coupled high-frequency plasma torch. These atoms could become further ionized into an ionic state under the high temperature and ionization conditions of the plasma. This process results in the atoms and ions being excited and emitting light from a light source. By using a spectroscopic instrument, the light emitted into the light source is broken down into a spectrum organized by wavelength. The purpose of this step is to acquire spectrum data regarding the particular wavelengths that the sample emits. By identifying the spectral wavelengths obtained, the sample is qualitatively analyzed after the spectra are detected using an

optoelectronic device. In parallel, a quantitative analysis is carried out using the light's intensity as a basis.

3.2.4 Brunauer Emmett Teller (BET) Specific Surface Area (SSA)

The surface area of a catalyst is a crucial factor influencing its performance. A larger surface area typically provides more active sites for chemical reactions, enhancing the catalyst's effectiveness. Consequently, precise and accurate measurement of the surface area is essential for optimizing catalyst design and ensuring reliable performance in various applications, from industrial processes to environmental protection. Accurate measurement techniques, such as the Brunauer-Emmett-Teller method, are therefore critical to understanding and improving catalyst efficiency. The Brunauer-Emmett-Teller (BET) method is a widely used technique to measure the specific surface area (SSA) of materials. This method is based on the physical adsorption of gas molecules onto the surface of a material.

Volumetric adsorption is commonly used for the estimation of BET surface area. The dynamic flow approach involves cooling a sample using a coolant, such as liquid nitrogen, while supplying an adsorbate gas with a specified concentration, such as 30% nitrogen diluted in helium. The adsorbate is absorbed by the sample, creating a drop in the concentration of the adsorb gas in the gas mixture. This decrease can be measured by analyzing the fluctuation (peak) in the signals from the detector (TCD). When adsorption approaches equilibrium, the concentration of gas which has been

adsorbed in the gas mixture reverts to its initial value, resulting in the TCD signals returning to their baseline. If cooling is stopped at this point (Dewar moves down), the adsorbate is desorbed from the sample.

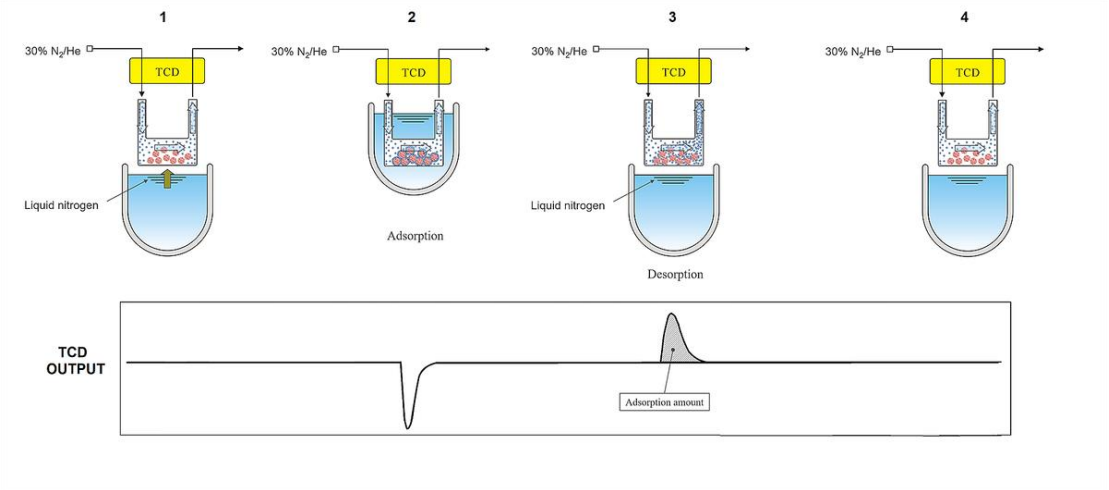


Figure 15. Schematic diagram of BET theory[37]

During this process, the concentration of the adsorbate gas temporarily rises in the mixture, triggering a peak in the thermal conductivity detector (TCD). Once desorption concludes, TCD signals revert to baseline. Due to its sharper profile and suitability for precise integration, the desorption peak is commonly employed for calculating specific surfaces.

The BET model can be shown by **Equation 6**. Here is the meanings of the parameter: p (pressure at equilibrium), p_0 (saturated vapor pressure of the adsorbed gas at the given temperature), V_m (volume of gas required to form a monolayer on the surface), V (amount of adsorption at pressure p), and C (a constant)[38].

Utilizing **Equation 7** which relates to surface area, it becomes possible to calculate the specific surface area. The equation incorporates N_A (Avogadro constant), s (adsorption cross-sectional area of the adsorbed species), and V_m (molar volume of the adsorbed species), V (quality of the adsorbent material)[38].

$$\frac{P}{V(p_0-p)} = \frac{1}{V_m C} + \frac{C-1}{V_m C} \times \frac{p}{p_0} \quad (6)$$

$$S_{BET} = \frac{(V_m N_A s)}{V} \quad (7)$$

3.3 Flow system and reaction test

3.3.1 Flow system configuration

The reactor system (**Figure 16**) which houses the reactor, includes a programmable muffle furnace (KSL-1100X Muffle Furnace, MTI Corporation). A K type thermocouple (1/8″, Omega Engineering) was inserted through the outlet tube so that the thermocouple tip is in contact with the catalyst bed. Feed flow rates were regulated by mass flow controllers (EL-FLOW select mass flow controllers, HOSKIN SCIENTIFIC LIMITED), and pressure was managed by a mechanical back pressure regulator (Stainless Steel BP Regulator, Swagelok). An Agilent Technologies, 5182-9411 silica gel orange column from Fisher Scientific and a mist trap (SMC AFM40-N02-Z-A, SMC Corporation) were used to extract the water. The IR analyzer (IR-208, Infrared Industries, Inc., USA) was used to measure the dry basis concentrations of CO, CO_2, and CH_4 in the outlet stream. LabVIEW (National Instruments) was used to

control the entire flow system. Analog-to-digital converters (NI 9215, NI 9263, National Instruments) were used to continuously monitor and record the flow rates, pressure, temperature, and gas concentrations.

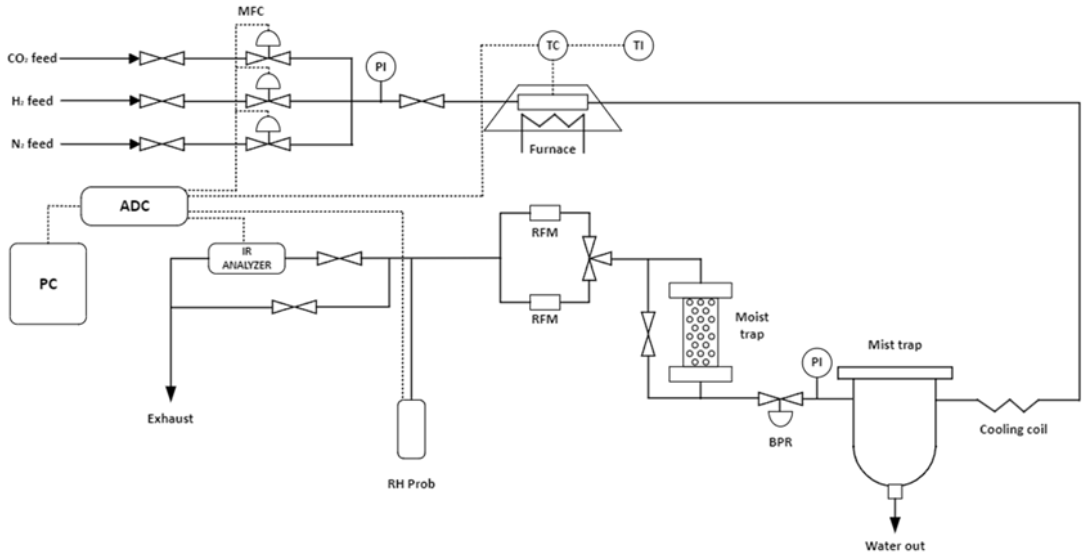


Figure 17. Flow system setup for conducting catalytic performance evaluation. Abbreviations: ADC, analog-to-digital converter; BPR, back pressure regulator; RFM, Rotor flow meter; IR, infrared; MFC, mass flow controller; PI, pressure indicator; PC, personal computer; TC, thermocouple; TI, temperature indicator.

3.3.2 Reactor configuration

For reaction tests, a stainless steel (SS) 1/4" tube was used **(Figure 18.)**. Pelletized and sieved catalysts (350-450 µm particle size) were loaded into the reactor through the either side of the SS tube sandwiched by quartz wool on both sides. Post reaction, the catalyst is then removed by removing the quartz wool for post reaction characterization test.

For stability tests, a 1/4" U-shaped quartz reactor was connected to SS flexible tubing and connected to the flow system. 400 mg of pelletized and sieved catalyst (350-450 µm) was fixed inside the reactor between quartz wool, then the reactor was placed inside the furnace.

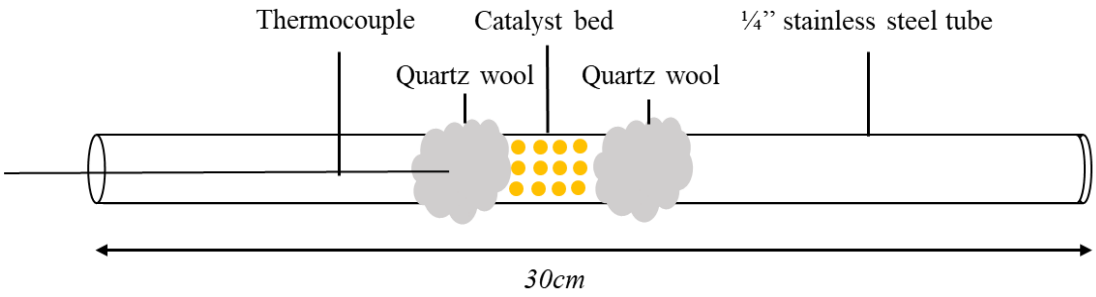


Figure 19. Stainless steel reactor schematic used for reaction tests

3.3.3 Reaction test and operating conditions

Prior to reaction tests, all catalysts were reduced under H_2 (200 mL/min at 600 °C for 2 h). After reduction, the feed was switched to a 3:1 mixture of H_2 and CO_2, and the temperature was reduced stepwise (25 °C step) in the 600-400 °C range (hold at 600 °C in the stability test). The duration of each step was 2 h to allow for complete stabilization of the IR signals for each temperature. All reported conversion and selectivity values were calculated under steady-state conditions (except for the stability test where transient data is reported).

CO_2 conversion and selectivity to CO were calculated according to Eqs. (8, 9) (y_{CO}, y_{CH_4}, and y_{CO_2} are mole fractions on dry basis, after removal of condensed water and humidity).

$$X_{CO_2} = \frac{y_{CO} + y_{CH_4}}{y_{CO_2} + y_{CO} + y_{CH_4}} \tag{8}$$

$$S_{CO} = \frac{y_{CO}}{y_{CO} + y_{CH_4}} \tag{9}$$

The carbon balance of the system is given by **Eq. (10)**. Where, α is the ratio of H_2/CO_2 in the feed, f_1 and f_2 are the conversion to CO and CH_4 respectively, $F_{C,out}$ is the outlet molar flow rate [39].

$$CB = (y_{CO_2} + y_{CO} + y_{CH_4})(1 + \alpha - f_1 - 4f_2) \tag{10}$$

$$\alpha = \frac{F_{H_{2,f}}}{F_{CO_{2,f}}} \tag{11}$$

$$f_1 = \frac{y_{CO}}{y_{CO_2} + y_{CO} + y_{CH_4}} \equiv \frac{F_{CO,out}}{F_{C,out}} = \frac{F_{CO,out}}{F_{CO_2,f}} \tag{12}$$

$$f_2 = \frac{y_{CH_4}}{y_{CO_2} + y_{CO} + y_{CH_4}} \equiv \frac{F_{CH_4,out}}{F_{C,out}} = \frac{F_{CH_4,out}}{F_{CO_2,f}} \tag{13}$$

Chapter 4: Catalyst performance and characterization

4.1 Structure and composition of fresh and spent catalysts

Table 1 lists the atomic loading (m) of M-doped (M=Fe, Ni, Co, and Cu) as determined by ICP-OES. The final loading values measured by ICP-OES may be due to the different precursors of the metals and the washing process may result in different amounts of precipitation loss.

Table 1 Specific surface area of fresh catalysts, particle size determined from XRD patterns of fresh and spent catalysts, and the activation energy determined from reaction tests.

Samples	M/(M+Ce) wt%	M/(M+Ce) at%	Fresh catalysts				Spent catalysts		$E_{a,rxn}$ (kJ/mol)
			SSA m^2/g	STD	D_{XRD}, nm	STD	D_{XRD}, nm	STD	
CeO_2	0.0	0.0	55.0	0.4	8.4	0.2	30.0	19.0	75.3
1.3FeCe	0.5	1.3	75.4	0.4	8.4	0.6	19.0	2.3	106.6
6.1FeCe	2.5	6.1	85.2	0.3	7.4	0.5	16.9	9.3	107.3
17FeCe	7.5	17.0	89.5	1.0	8.5	1.0	18.8	5.3	80
2.1CoCe	0.9	2.1			10.3	0.0	25.5	21.0	68.5
4.6CoCe	2.0	4.6			9.6	0.1	26.9	2.8	43.2
11CoCe	4.9	11.0	42.1	0.2	9.8	0.8	27.0	2.1	33.6
0.8NiCe	0.3	0.8			13.4	0.4	29.1	14.6	68.5
8.8NiCe	3.9	8.8			9.1	0.0	17.4	5.8	37.3
12.8NiCe	5.8	12.8	42.9	0.2	10.1	0.1	18.9	6.2	42.3
0.5CuCe	0.2	0.5			10.8	0.3	20.1	1.3	98.4
2.2CuCe	1.0	2.2			9.3	0.5	20.3	10.7	113.9
5.8CuCe	2.7	5.8	77.2	0.4	8.6	0.7	19.4	4.9	124.5

The X-ray diffraction (XRD) patterns of the fresh and spent mMCe catalysts are presented in **Figure 18** and **Figure 19**, respectively. Notably, no separate metal or metal oxide phases were detected in any of the catalysts. Instead, the XRD patterns for both fresh and spent catalysts consistently matched the CeO_2 fluorite structure, as

referenced by the Powder Diffraction File (PDF 00-034-0394). The characteristic peaks for this structure were observed along the (111), (200), (220), (311), (222), (400), (331), and (420) planes. This observation suggests that the metals have integrated into the CeO_2 lattice, replacing Ce ions, which is particularly evident at low metal loadings.

It is important to highlight that the absence of detectable Fe species in the 17FeCe catalyst, as shown in **Figures 18a** and **19a**, might be attributed to the formation of atomic-level-sized Fe clusters on the surface of CeO_2. These clusters are so small that they fall below the detection limit of XRD. Additionally, a significant amount of Fe could dissolve into the CeO_2 lattice, making it undetectable by XRD when examining the surface. This indicates that the Fe species are well incorporated into the CeO_2 matrix, further confirming the substitution of Ce ions by Fe at the atomic level. This incorporation is more pronounced at higher Fe loadings, where Fe is integrated into the lattice rather than forming distinct phases.

The particle sizes got from the XRD peaks are show in **Table 1**. Initially, the fresh catalysts display relatively small particle sizes, averaging around 10 nm. However, after the reaction, there is a significant increase in particle size, with a 2-3-fold increment observed. Despite particle size increase, the average particle size of the spent catalysts remains below 30 nm, indicating that while growth occurs, it is controlled.

A notable observation is that the larger increment in particle size seen in pure CeO_2 compared to the metal-doped catalysts. This suggests that the doping of metals plays a crucial role in inhibiting the sintering effect during the reaction process. The presence of metal dopants seems to stabilize the structure, preventing the particles from growing excessively and thus maintaining a more consistent size distribution even after the reaction.

Furthermore, **Table 1** also presents the specific surface areas (SSA) of selected samples. A comparison reveals that the SSAs of mFeCe and mCuCe are significantly higher than that of pure CeO_2. This enhancement in surface area upon the addition of Fe and Cu indicates that these metals not only prevent excessive particle growth but also contribute to maintaining a larger surface area, which is beneficial for catalytic activity. On the other hand, the SSAs for mNiCe and mCoCe are found to be lower than that of pure CeO_2. This suggests that the incorporation of Ni and Co does not have the same stabilizing effect on the surface area as Fe and Cu. Instead, these metals might lead to a different structural modification, resulting in a reduction of the surface area compared to the pure CeO_2.

The variations in particle size and surface area show the significant impact of metal doping on the physical properties of CeO_2-based catalysts. The ability of Fe and Cu enhance surface area while controlling particle growth highlights their potential

advantage in catalytic applications, where high surface area is often correlated with increased activity.

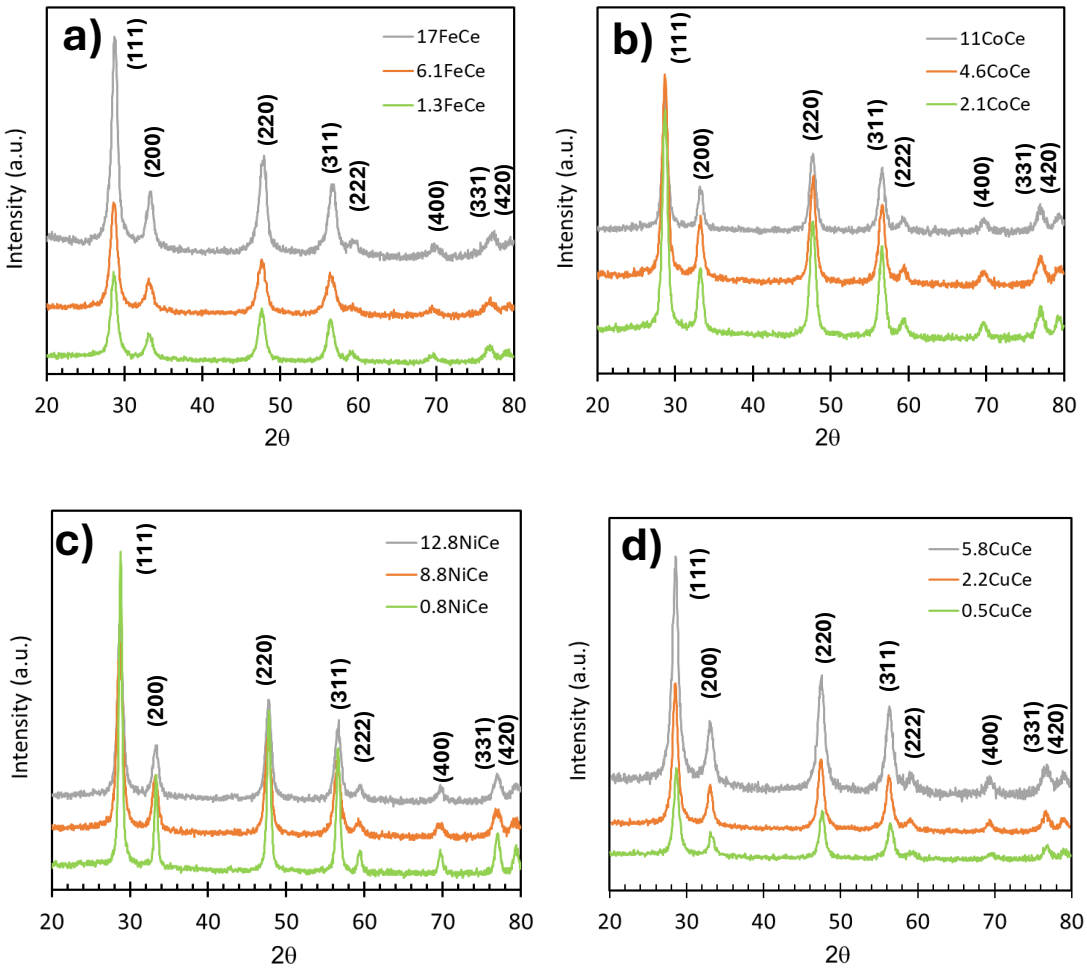


Figure 20. XRD patterns of fresh a) $FeCeO_2$, b) $CoCeO_2$ catalysts; c) $NiCeO_2$ catalysts, d) $CuCeO_2$ catalysts.

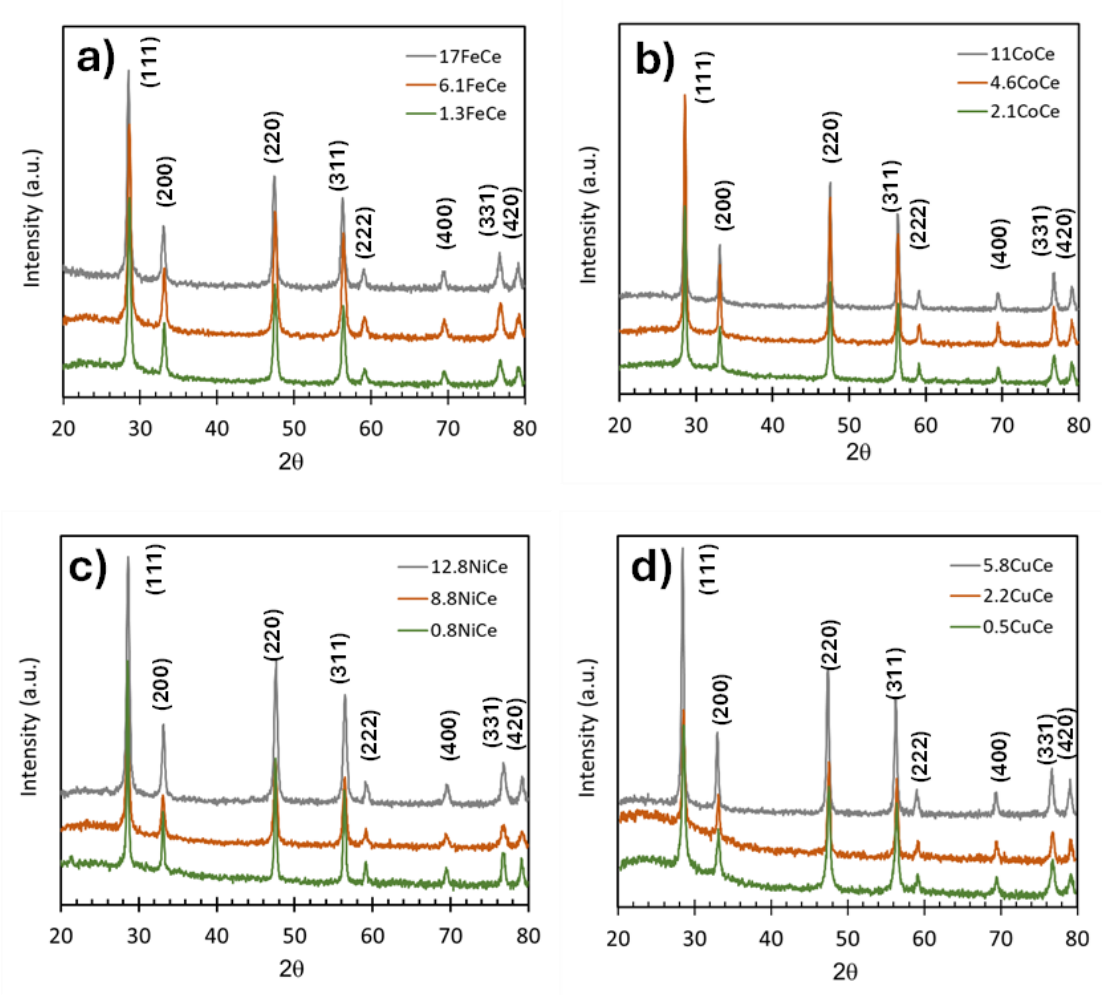


Figure 21. XRD pattern of spent a) $FeCeO_2$, b) $CoCeO_2$ catalysts; c) $NiCeO_2$ catalysts, d) $CuCeO_2$ catalysts.

4.2 CO_2 TPD adsorption strength analysis

The CO_2-temperature programmed desorption (CO_2-TPD) profiles of the fresh catalysts are illustrated in **Figure 20**, with the deconvoluted peaks for individual samples displayed in **Figure 21**. In these profiles, peaks centered below 150 °C are attributed to the desorption of weakly adsorbed CO_2, which corresponds to physiosorbed CO_2.

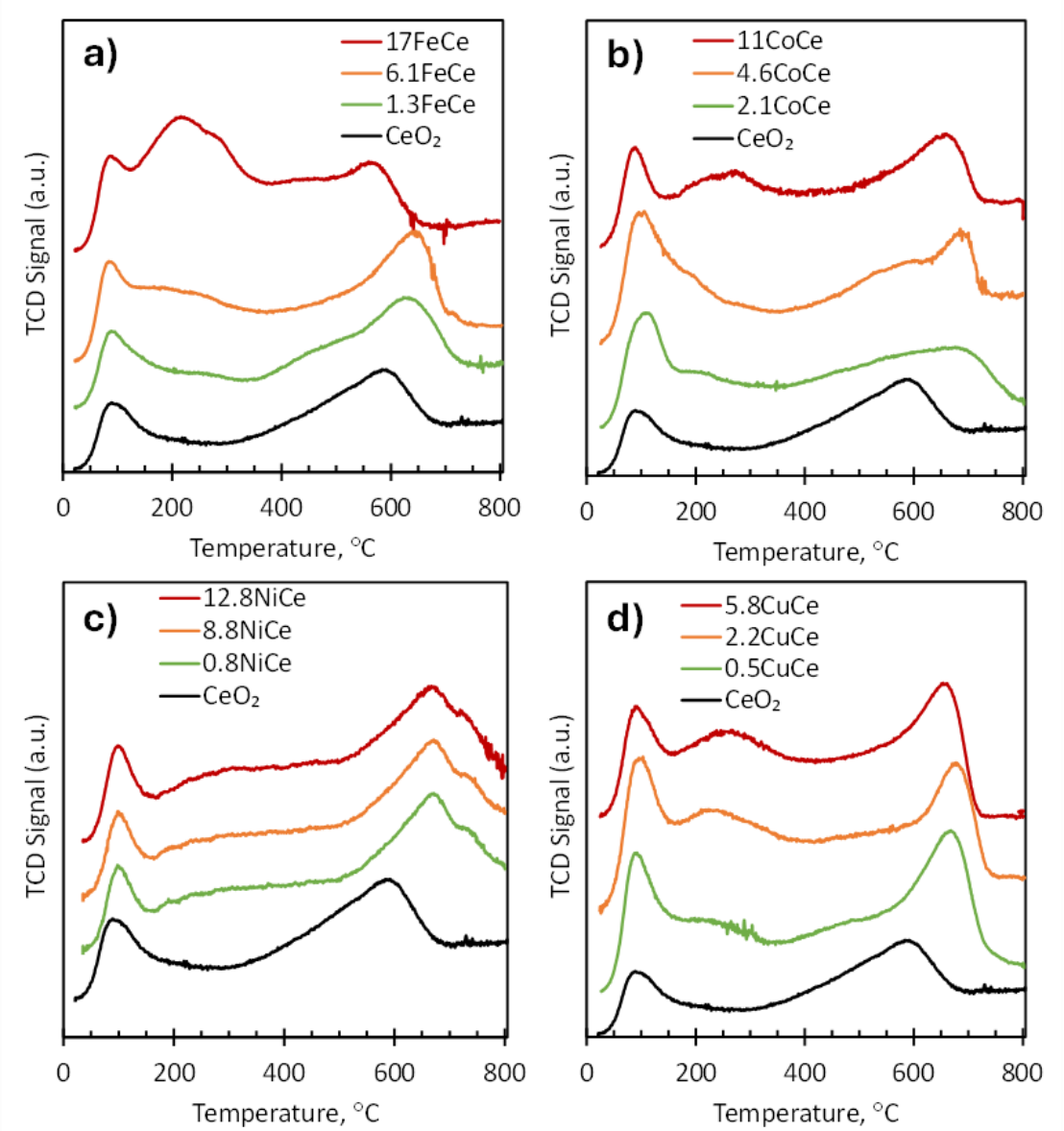


Figure 22. CO_2-TPD patterns of fresh a) $FeCeO_2$, b) $CoCeO_2$, c) $NiCeO_2$, d) $CuCeO_2$ catalysts.

For the Cu-doped catalysts, two distinct peaks are observed in the weak adsorption region. The first peak, occurring at the lowest temperature, is attributed to the weak adsorption of CO_2 on sites located within the CeO_2 regions of the catalyst surface. The

second peak, appearing at a slightly higher temperature, is indicative of CO_2 adsorption on sites modified by the doping material.

This differentiation in adsorption sites highlights the impact of Cu doping on the catalyst surface. The presence of two peaks suggests that Cu introduction creates additional adsorption sites or modifies existing ones on the CeO_2 surface. The peak at the lower temperature remains consistent with the weak adsorption behavior typical of pure CeO_2 regions, while the peak at the higher temperature points to a modified environment where the interaction between CO_2 and the surface is altered due to the presence of Cu.

These findings emphasize the role of doping materials in changing the adsorption properties of catalysts. By creating or modifying adsorption sites, dopants like Cu can influence the distribution and strength of CO_2 adsorption. This, in turn, can affect the overall catalytic performance, as adsorption characteristics are crucial for reactions involving CO_2.

The CO_2-TPD profiles reveal a moderate peak in each sample, located between 150-300 °C, which corresponds to CO_2 absorbed on intermediate-strength sites on the surface. These sites are considered to be the active sites for the reverse water gas shift (RWGS) reaction. Notably, this moderate peak shifts to higher temperatures as the catalysts are doped with transition metals. For instance, the peak shifts from 174.2 °C

on pure CeO_2 to 261.5 °C on 12.8NiCe. All doped samples exhibit higher desorption temperatures compared to pure CeO_2.

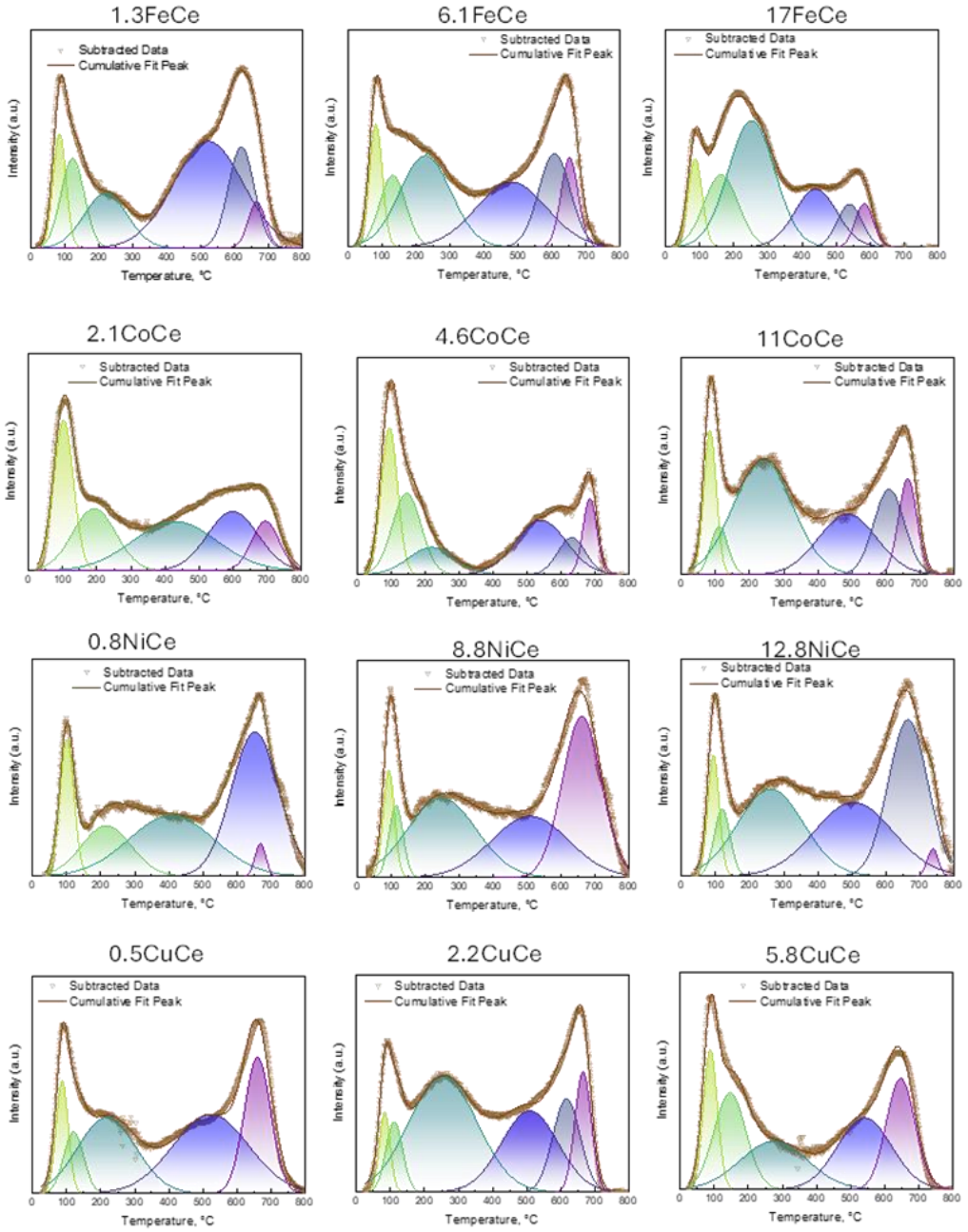


Figure 23. CO_2-TPD patterns and the deconvoluted adsorption peaks of fresh metal doped CeO_2 catalysts

Additionally, the intensity of this peak increases with the metal loading, as shown in **Figure 22**. This observation suggests that the CO_2 adsorption strength at these intermediate binding energy sites is enhanced when the CeO_2 surface is modified with transition metals such as Cu, Fe, Ni, and Co. This enhancement likely contributes to the improved catalytic performance for the RWGS reaction.

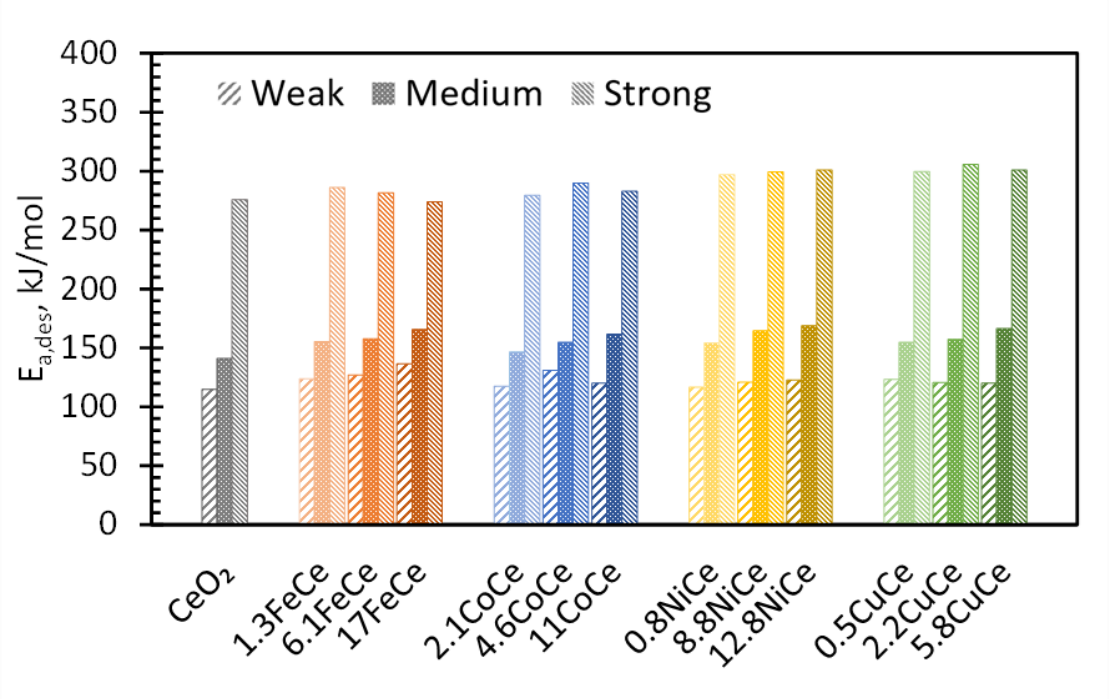


Figure 24. Activation energy of desorption of weak, medium and strong adsorbed CO_2 on metal doped CeO_2 surfaces calculated from CO_2-TPD

Table 2 Metal loading, activation energy of desorption of weak, intermediate, and strong peaks calculated from CO_2-TPD and the corresponding peak positions.

Samples	M/(M+Ce) wt%	M/(M+Ce) at%	$E_{a,des,weak}$ (kJ/mol)	$T_{a,des,weak}$ (°C)	$E_{a,des,medium}$ (kJ/mol)	$T_{a,des,medium}$ (°C)	$E_{a,des,strong}$ (kJ/mol)	$T_{a,des,strong}$ (°C)
CeO_2	0.0	0.0	115.0	94.5	141.2	174.2	275.8	589.1
1.3FeCe	0.5	1.3	123.8	122.0	155.3	219.7	286.0	620.4
6.1FeCe	2.5	6.1	127.0	132.0	157.9	227.7	281.6	606.9
17FeCe	7.5	17.0	136.6	161.8	165.6	251.5	274.1	584.0
2.1CoCe	0.9	2.1	117.5	192.2	146.5	192.2	279.4	600.2
4.6CoCe	2.0	4.6	131.1	144.8	154.9	218.5	289.9	632.1
11CoCe	4.9	11.0	120.0	110.2	161.5	238.9	282.8	610.5
0.8NiCe	0.3	0.8	154.3	216.5	154.3	216.5	297.1	654.0
8.8NiCe	3.9	8.8	121.0	113.2	164.6	248.3	299.3	660.7
12.8NiCe	5.8	12.8	122.8	118.9	168.9	261.6	301.0	666.0
0.5CuCe*	0.2	0.5	123.2	120.1	154.8	218.2	299.5	661.5
2.2CuCe*	1.0	2.2	120.5	111.7	157.2	225.5	305.5	679.7
5.8CuCe*	2.7	5.8	120.2	110.7	166.5	254.4	301.0	666.0

High-temperature peaks, observed above 600 °C, are attributed to the adsorption of species with higher binding energies and the reduction of CO_2 to CO on the surface. **Figure 22** summarizes the activation energies of desorption calculated from the peaks corresponding to weak, moderate, and strong CO_2 adsorption sites. The values of the activation energies of desorption ($E_{a,des}$) and the peak positions are listed in **Table 2.**

The trend for the intermediate peak is clear: the introduction of transition metals enhances the CO_2 adsorption strength, and the activation energy of desorption increases with the metal loading. For weak and strong adsorption peaks, no clear trend is observed. However, in general, the mNiCe and mCuCe samples show higher activation energies for the strong adsorption peaks, indicating stronger CO_2 binding at these sites.

These findings highlight the significant influence of transition metal doping on the CO_2 adsorption characteristics of CeO_2-based catalysts. By altering the adsorption strength and increasing the activation energies of desorption, the doped catalysts demonstrate improved potential for applications in reactions involving CO_2.

4.3 Catalytic performance evaluation

4.3.1 Catalytic performance of Fe-CeO_2

During all the reaction experiments, the catalyst was first reduced at 600 °C with pure H_2 flow at the rate of 200 mL/min for 2 hours, when the atmosphere was switched to a CO_2/H_2 mixture. Throughout all the experiments, the H_2/CO_2 feed ratio was kept constant at 3, and the pressure was maintained at 3 bar (absolute pressure). The catalytic performance of pure CeO_2 and mMCe catalysts was tested within the temperature range of 400 – 600°C with a fixed space velocity of 60,000 mL/h. Each temperature or space velocity step lasted for at least 2 hours with a temperature gradient of 25°C, and data were recorded once the IR signal was fully stabilized.

Figure 23 indicates the conversion of CO_2 to CO as a function of temperature on metal doped CeO_2 catalysts and **Figure 24** presents the selectivity to CO on each catalyst. $FeCeO_2$ displayed an increased conversion at all temperatures when compared to undoped pure CeO_2 (gray markers in **Figure 23a**). At the same time, the conversion rate of CO_2 increased with the increase of the load. The CO_2 conversion

was higher in samples with a higher Fe concentration (17FeCe) than in samples with a lower Fe content (6.1FeCe and 1.3FeCe). Furthermore, the high loading conversion of $FeCeO_2$ was more noticeable at higher temperatures; for example, the 17FeCe catalyst showed the highest CO_2 conversion (56%) at 600 °C. The selectivity to CO was 100% since during the reaction, the only product seen in the exit stream was CO (**Figure 23a**). This suggests that superior selectivity of CeO_2 to CO might not be affected by the addition of Fe.

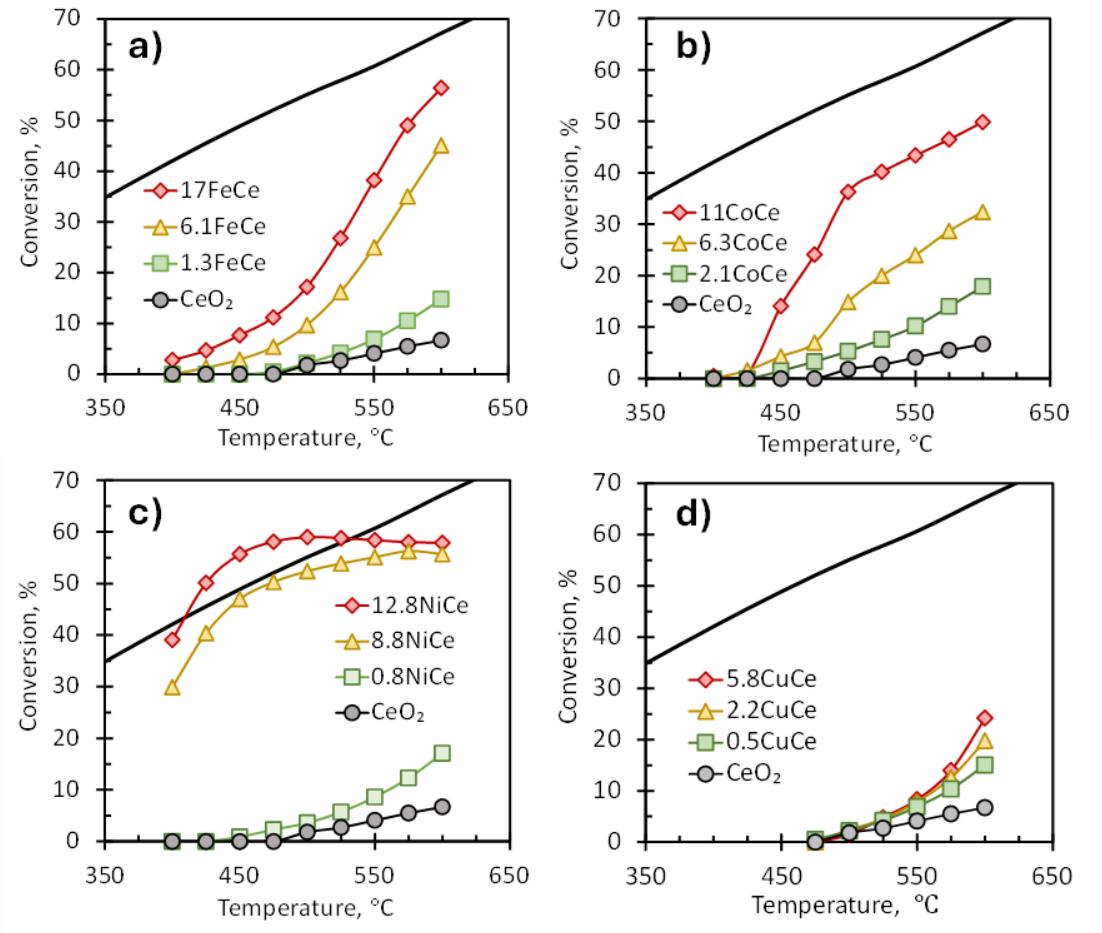


Figure 25. a) CO_2 conversion as a function of temperature (400-600°C) a) $FeCeO_2$, b) $CoCeO_2$, c) $NiCeO_2$, d) $CuCeO_2$ catalysts. Condition: GHSV =

60,000 mL $h^{-1}gcat^{-1}$, H_2/CO_2 = 3:1, P = 3 bar (absolute). The solid black line represents the of RWGS. Red diamond, yellow triangle and green square represent the high, medium and loading $MCeO_2$ catalysts respectively.

equilibrium curve

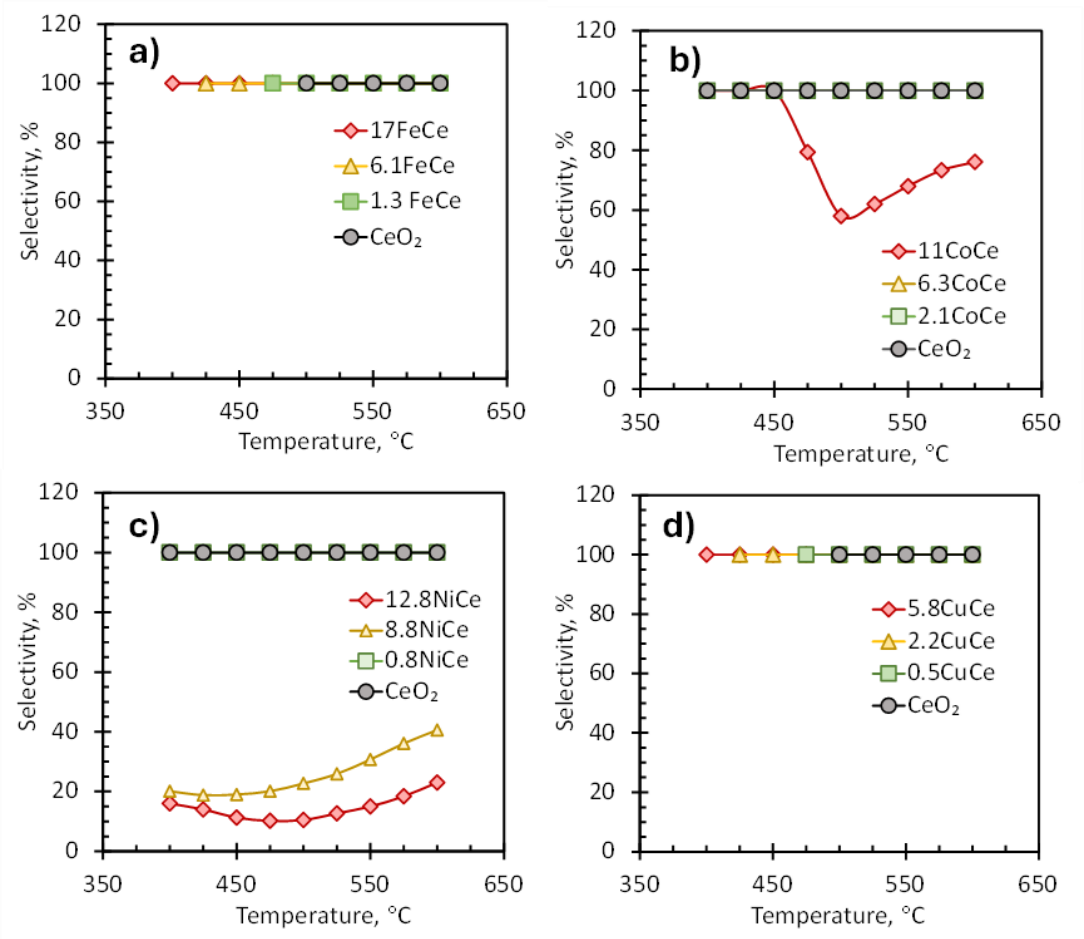


Figure 26. Selectivity towards CO as a function of temperature of a) $FeCeO_2$, b) $CoCeO_2$, c) $NiCeO_2$, d) $CuCeO_2$ catalysts. Condition: GHSV = 60,000 mL $h^{-1}gcat^{-1}$, H_2/CO_2 = 3:1, P = 3 bar (absolute). Red diamond, yellow triangle and green square represent the high, medium and loading $MCeO_2$ catalysts respectively.

Arrhenius plots for pure CeO_2 and $FeCeO_2$ catalysts shown in **Figure 27a** was obtained by a separate set of reactions tests. CO generation rates were calculated from **Eq. (21)** and activation energy estimation was done using **Eq. (22).**

$$R_{CO} = \frac{F_{CO_2,f} X_{CO_2}}{W_C} \tag{21}$$

$$\ln(R_{CO}) = \ln(A) - \frac{E_{a,rxn}}{R_g T} \tag{22}$$

From the Arrhenius plot (the **Figure 25**), Activation energy of CeO_2 ,17FeCe, 6.1FeCe and 1.3Ce can be know which is 75.3 kJ/mol, 80 kJ/mol, 107.3 kJ/mol, 106.6 kJ/mol. Activation energy estimation showed that increasing Fe loading will decrease the activation energy of reaction, thus facilitate the reaction.

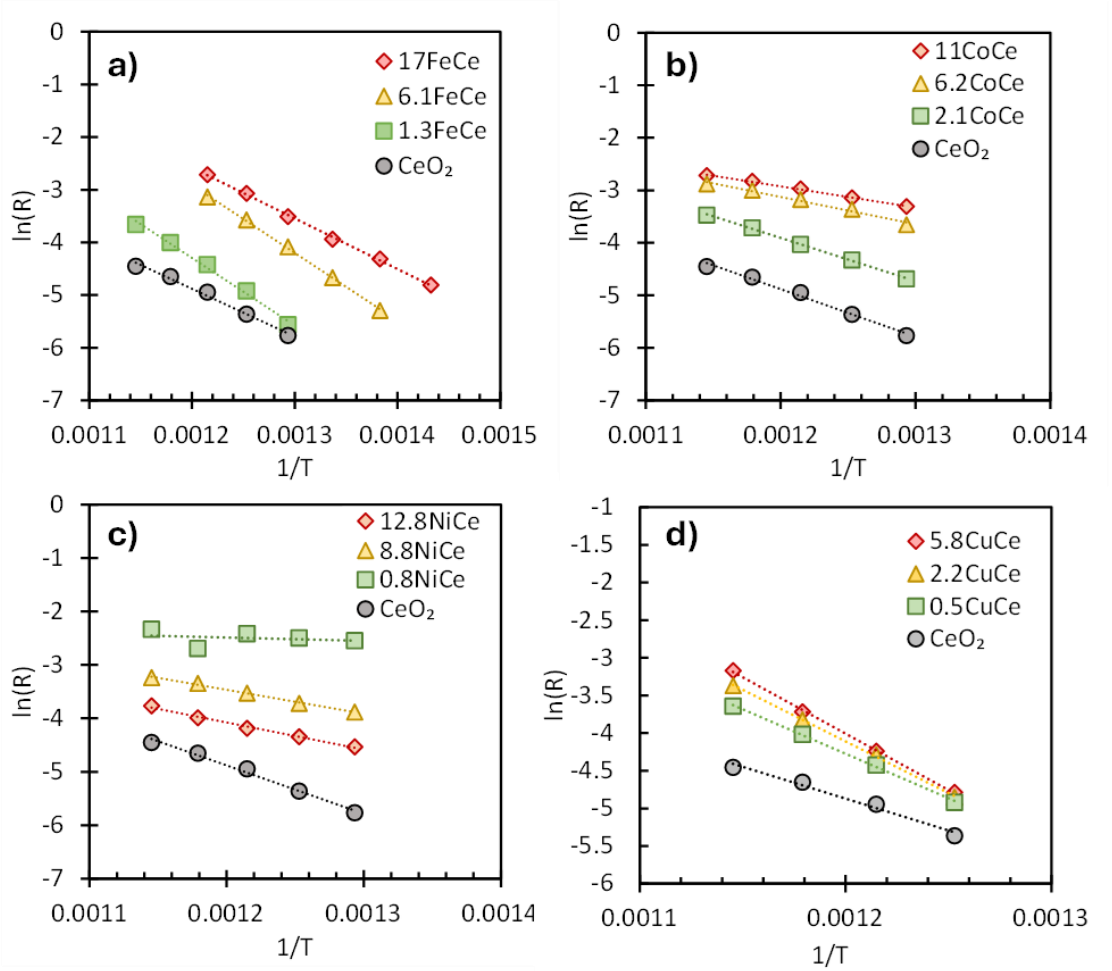


Figure 28.Selectivity towards CO as a function of temperature of a) $FeCeO_2$, b) $CoCeO_2$, c) $NiCeO_2$, d) $CuCeO_2$ catalysts. Condition: GHSV = 60,000 mL $h^{-1}gcat^{-1}$, H_2/CO_2 = 3:1, P = 3 bar (absolute). Red diamond, yellow triangle and green square represent the high, medium and loading $MCeO_2$ catalysts respectively.

4.3.2 Catalytic performance of Co-CeO_2

Compared to undoped pure CeO_2 (gray markers in **Figure 23b**), $CoCeO_2$ conversion increased at all temperatures. At the same time, the conversion rate of CO_2 increased with the increase of the load. The CO_2 conversion of samples with higher

Co concentrations (11CoCe) was higher than that of samples with lower Co concentrations (6.3CoCe and 2.1CoCe). Furthermore, the high loading conversion of $CoCeO_2$ was more noticeable at higher temperatures; for example, the 11CoCe catalyst showed the highest CO_2 conversion (49%) at 600 °C.

When the loading of samples is low, the selectivity to CO was 100% since during the reaction, the only product seen in the exit stream was CO (**Figure 24b**). This also suggests that superior selectivity of CeO_2 to CO might not be affected by the addition of Co. But when the loading is higher ,for example, the 11CoCe the selectivity to CO decrease significantly with the temperature raise and increase after about 500 ℃. By IR it can be known that in addition to CO generation, a large amount of methane is generated as a by-product. This is a result of the low temperatures of 450 - 550 °C, which favor the methanation reaction.

The Arrhenius plot (**Figure 25b**) provides insight into the activation energies for different catalysts: CeO_2, 11CoCe, 6.3CoCe, and 2.1CoCe, which are 75.3 kJ/mol, 33.6 kJ/mol, 43.2 kJ/mol and 68.5 kJ/mol, respectively. The reaction rate of RWGS on 11CoCe is calculated by the conversion of CO_2 towards CO only, the conversion to CH_4 was excepted. This data indicates a clear trend: increasing the Co loading in the catalysts significantly lowers the activation energy required for the reaction. Consequently, the reaction becomes more efficient and proceeds more readily with

higher Co content. This relationship highlights the beneficial effect of Co on enhancing catalytic performance by reducing the energy barrier.

4.3.3 Catalytic performance of Ni-CeO_2

Figure 23c also showed the same law, with the increase of the Ni loading, the CO_2 conversion raising. At the same time, the conversion rate of CO_2 increased with the increase of the load.

When the sample loading is low, the selectivity to Ni is 100%, as CO is the only product observed in the exit stream during the reaction (**Figure 24c**). This indicates that the high selectivity of CeO_2 to CO is not influenced by the addition of Ni. However, with higher loadings, such as 12.8NiCe, the selectivity to CO decreases significantly as the temperature rises but increases again above 500°C. IR analysis reveals that at lower temperatures (450 - 550°C), in addition to CO, a substantial amount of methane is produced as a by-product, due to the methanation reaction being favored at these temperatures.

The Arrhenius plot (**Figure 25c**) shows the activation energies for various catalysts: CeO_2, 12.8NiCe, 8.8NiCe, and 0.8NiCe, measured at 75.3 kJ/mol, 42.3 kJ/mol, 37.3 kJ/mol and 68.5 kJ/mol, respectively. The reaction rate of RWGS on 8.8NiCe and 12.8NiCe are calculated by the conversion of CO_2 towards CO only, the conversion to CH_4 was excepted. This trend demonstrates that increasing the Ni loading in the

catalysts results in a significant decrease in activation energy. Lower activation energy means the reaction can occur more easily and efficiently. Thus, higher Ni content in the catalyst enhances its performance by reducing the energy barrier needed for the reaction to proceed.

4.3.4 Catalytic performance of Cu-CeO_2

Figure 24d illustrates the conversion of CO_2 to CO as a function of temperature for different $CuCeO_2$ loadings. Throughout the reaction, CO was the only product detected in the outlet stream, resulting in 100% selectivity towards CO. This observation aligns with previous studies on pure CeO_2, indicating that the addition of Cu does not alter CeO_2's high selectivity for CO. Compared to undoped CeO_2 (represented by gray markers in **Figure 23d**), $CuCeO_2$ catalysts achieved higher CO_2 conversion rates at all temperatures. Notably, the catalyst with the highest Cu concentration (5.8CuCe) demonstrated superior CO_2 conversion compared to those with lower Cu loadings (0.5CuCe and 2.2CuCe). This enhanced performance was particularly evident at high temperatures, with the highest CO_2 conversion of 24.2% observed at 600°C on the 5.8CuCe catalyst.

The Arrhenius plot (**Figure 25d**) reveals the activation energies for different catalysts: CeO_2, 5.8CuCe, 2.2CuCe, and 0.5CuCe, with values of 75.3 kJ/mol, 124.5 kJ/mol, 113.9 kJ/mol, and 98.4 kJ/mol, respectively. Interestingly, the Cu-doped CeO_2

catalysts exhibited an inverse trend compared to other dopants. As the Cu loading increased, the activation energy also increased, indicating a higher reaction barrier.

4.3.5 Comparison of the performance of all catalysts

The 17FeCe catalyst, with the highest Fe loading, exhibited the highest CO_2 conversion of 56% compared to catalysts with lower Fe loadings, as shown in **Figure 23**. For Fe and Cu-doped CeO_2 catalysts, as well as low-loading Co and Ni-doped CeO_2 (2.1CoCe, 6.3CoCe, and 0.8NiCe), the selectivity to the reverse water gas shift (RWGS) reaction remained at 100%, with CO being the only product detected in the outlet stream. This consistency with previous observations of pure CeO_2's 100% selectivity indicates that introducing Cu, Fe, Co, and Ni at low loadings does not affect CeO_2's superior selectivity for CO. However, when Co and Ni loadings were higher (11CoCe, 8.8NiCe, and 12.8NiCe), a significant amount of CH_4 was produced alongside CO, particularly at lower temperatures in the 450 - 550°C range, where the methanation reaction is favored. For mNiCe, increased Ni loading resulted in more CH_4 production, with CH_4 becoming the dominant product at 500 °C. As the temperature increased, the selectivity gradually shifted back to CO. Compared to undoped CeO_2 shown in **Figure 23**, all doped catalysts exhibited higher conversion rates at all temperatures.

The activation energy of reaction calculated from reaction tests versus the loading are shown in **Figure 26**, and it is clear that, for Fe, Ni and Co, increase the metal

loading will decrease the activation energy of reaction, thus facilitate the reaction. However, Cu doped CeO_2 exhibited a reversed trend that a greater reaction barrier was observed when the Cu loading was higher.

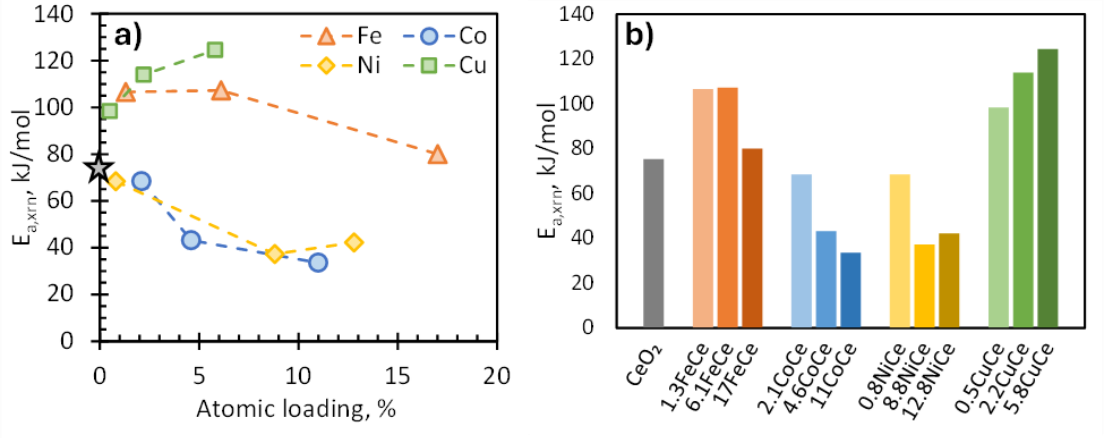


Figure 29. a) $E_{a,rxn}$ as a function of transition metal loading and star represents pure CeO_2; b) Experimental activation energy ($E_{a,rxn}$) for different mMCe catalysts

4.4 Correlation between activation energy and desorption energy

To investigate the correlation between activation energy ($E_{a,rxn}$) and activation energy of CO_2 desorption ($E_{a,des}$), as presented in **Figure 27**, $E_{a,rxn}$ was plotted as a function of $E_{a,des}$ that corresponding to the medium strength peak. For mCoCe and mNiCe, there is a negative correlation observed that with the increase of $E_{a,des}$, $E_{a,rxn}$ decreased, which also indicates that the CO_2 reduction was facilitated. This finding supports that on Co and Ni doped CeO_2, the CO_2 binding strength indicates the activation of CO_2 which is highly related to the $E_{a,rxn}$. However, a reverse trend was observed for Cu and Fe as shown in **Figure 27** which higher $E_{a,des}$ corresponding to

elevated $E_{a,rxn}$ as indicated. The outlier of 17FeCe could be due to the large extent of modification of CeO_2 surface caused by the high Fe loading.

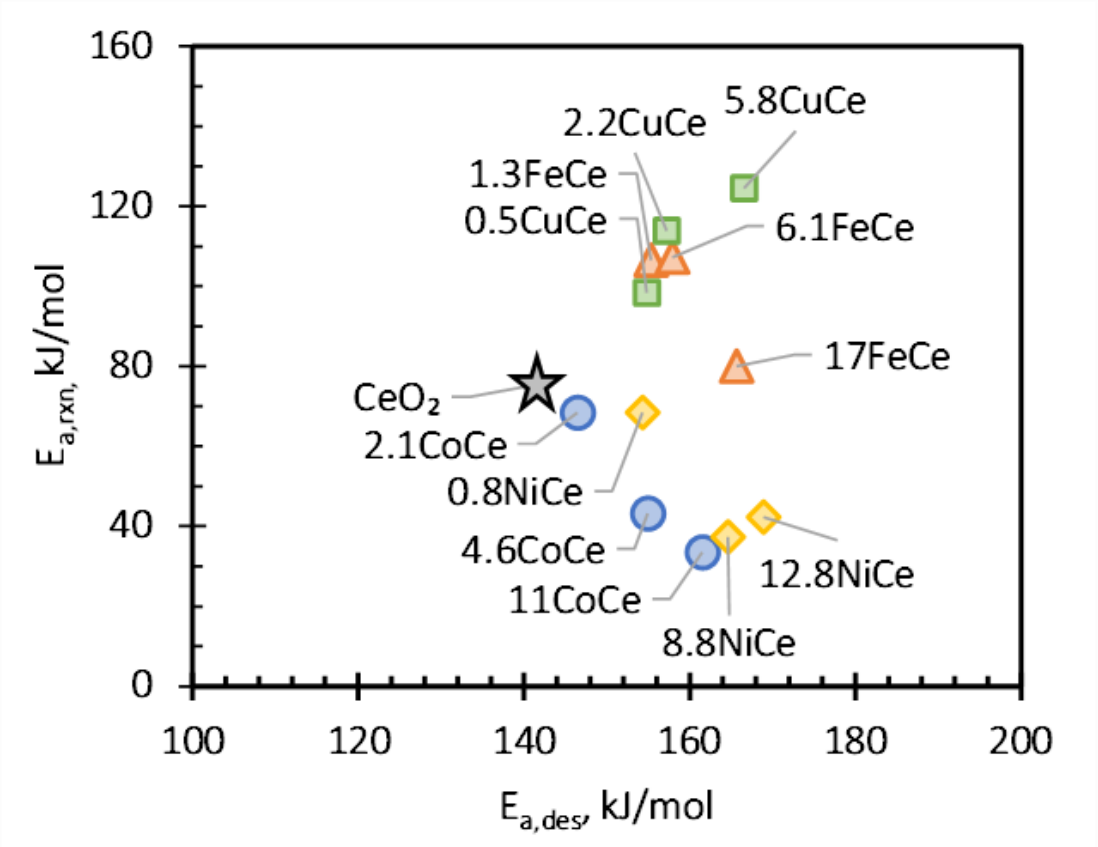


Figure 30. Activation energy measured from performance tests ($E_{a,rxn}$) as a function of activation energy of CO_2 desorption from the medium strength site ($E_{a,des}$). Star represents pure CeO_2.

Chapter 5: Conclusion and future work

5.1 Conclusions

The successful investigation of thermocatalytic conversion involved studying the catalytic activity of transition metal doped ceria catalyst. $MCeO_2$ catalysts (M = Fe, Co, Ni and Cu) with varying transition metal doping concentrations were successfully synthesized using the direct precipitation method and evaluated for the reverse water gas shift reaction. XRD showed no separate phase of transition metal and transition metal oxides suggesting successful doping into the lattice. Reaction tests conducted within a specific temperature range have demonstrated significant findings regarding $FeCeO_2$ and $CuCeO_2$ catalysts. Additionally, the tests revealed an important trend: as the doping concentration of the catalysts increases, their activity also improves. This means that by increasing the amount of Fe or Cu in the CeO_2, the catalysts become more efficient in facilitating the reaction. This enhancement in catalytic activity with higher doping levels suggests potential for optimizing these materials for industrial applications where selective CO reactions are crucial.

Additionally, the observed linear trend between $E_{a,des}$ and $E_{a,rxn}$ suggests that CO_2 adsorption and activation play a crucial role in reducing the activation energy of the overall reaction. Enhanced adsorption strength increases the availability of vacant active sites, contributing to superior catalyst performance. Consequently, copper

doping induces active sites on the catalyst surface, resulting in stronger CO_2 adsorption and enhancing the performance of the $CuCeO_2$ catalyst.

This study highlights the versatility of CeO_2 as a catalyst in the reverse water gas shift (RWGS) reaction for several reasons. The structure of CeO_2 can be modified through metal doping, which enhances its catalytic activity by introducing additional active sites, as demonstrated in the $CuCeO_2$ experiments. Overall, these characteristics make CeO_2 a highly promising catalyst for the RWGS reaction, especially in harsher conditions where catalyst performance and stability are vital. Its versatility, modified structure through doping, and compatibility with support materials make CeO_2 an excellent candidate for catalytic applications in various industrial settings.

In summary, this study elucidates the relationship between CO_2 adsorption energies and the concentration of Fe, Co, Ni and Cu doped CeO_2 surfaces. The introduction of Fe, Ni and Cu atoms notably enhances CO_2 adsorption, evidenced by an increased in adsorption energy compared to pure CeO_2 surfaces. Specifically, the $2Cu/CeO_{2-x}(111)$ surface showed the highest adsorption energy. Co and Ni surfaces present relatively lower CO_2 activation, indicated by the lower adsorption energies. The present analysis underscores the significance of transition metal doping in enhancing CO_2 adsorption on CO_2 surfaces, with Cu and Fe showing particularly promising results. The correlations established between adsorption energies and reaction activation energies are critical to gain insights on catalytic performance.

Despite that the addition of Fe as a dopant does not lower the activation energy compared to pure CeO_2, laboratory experiments showed that the Fe dopant indeed promotes the conversion of CO_2. These findings highlight the complexities of heterogeneous catalytic processes and the challenges in predicting catalyst performance. Furthermore, this study emphasizes that the adsorption stability of dissociated CO_2 on the surface is paramount in determining the performance in terms of transition state energy since a more stable configuration will lead to lower activation energy.

5.2 Future Work

To further investigate the performance and potential applications of Fe and Cu catalysts, we propose a comprehensive series of additional tests, with a particular focus on stability testing. These catalysts have shown 100% CO selectivity, making it essential to understand their behavior and efficiency over extended periods of operation. Stability testing will provide critical insights into their long-term performance and reliability, which are key factors for practical deployment in industrial processes.

In addition to stability tests, employing in-situ FTIR (Fourier Transform Infrared Spectroscopy) techniques can offer valuable information about the intermediate products formed during the reaction. This real-time analysis can help elucidate the specific mechanisms at play, providing a deeper understanding of the catalytic

processes. Such insights are crucial for the rational design and optimization of catalysts, ensuring that they achieve the desired performance characteristics.

Furthermore, post-reaction thermogravimetric analysis (TGA) can be utilized to assess the extent of coking and sintering in the catalysts. This analysis will help determine how the catalysts degrade over time and under reaction conditions, providing data on their durability and operational lifespan. Understanding these aspects is essential for improving catalyst formulations and ensuring consistent performance in long-term applications.

Moreover, exploring alternative synthesis methods for these catalysts could lead to the development of materials with distinct morphological characteristics. Different morphologies can significantly influence catalyst properties, such as increasing surface area, enhancing conversion rates, and improving overall efficiency. Investigating new synthesis routes could therefore yield catalysts with optimized structures and superior performance.

The exploration of innovative synthesis techniques and their impact on catalyst morphology and performance represents a highly promising research direction. It could lead to significant advancements in catalyst technology, with the potential to enhance various industrial processes. This line of inquiry not only broadens our

understanding of catalyst behavior but also opens up new possibilities for improving their efficiency and effectiveness.

References

[1] IEA. CO_2 Emissions in 2023, 2024. Available: https://www.iea.org/reports/co2-emissions-in-2023

[2] Z. Liu, Z. Deng, S. J. Davis, C. Giron, and P. Ciais, "Monitoring global carbon emissions in 2021," Nature Reviews Earth & Environment, 3 (2022) 217-219.

[3] U. S. E. P. Agency. Sources of Greenhouse Gas Emissions, 2022. Available: https://www.epa.gov/ghgemissions/sources-greenhouse-gas-emissions

[4] D. S. Simakov, Renewable synthetic fuels and chemicals from carbon dioxide: fundamentals, catalysis, design considerations and technological challenges. Springer, 2017.

[5] S. Hernández, M. A. Farkhondehfal, F. Sastre, M. Makkee, G. Saracco, and N. Russo, "Syngas production from electrochemical reduction of CO_2: current status and prospective implementation," Green Chemistry, 19 (2017) 2326-2346.

[6] Y. A. Daza and J. N. Kuhn, "CO_2 conversion by reverse water gas shift catalysis: comparison of catalysts, mechanisms and their consequences for CO 2 conversion to liquid fuels," RSC advances, 6 (2016) 49675-49691.

[7] B. Lu and K. Kawamoto, "Preparation of mesoporous CeO_2 and monodispersed NiO particles in CeO_2, and enhanced selectivity of NiO/CeO_2 for reverse water gas shift reaction," Materials Research Bulletin, 53 (2014) 70-78.

[8] P. Panagiotopoulou, "Hydrogenation of CO_2 over supported noble metal catalysts," Applied Catalysis A: General, 542 (2017) 63-70.

[9] V. Lebarbier, R. Dagle, A. Datye, and Y. Wang, "The effect of PdZn particle size on reverse-water–gas-shift reaction," Applied Catalysis A: General, 379 (2010) 3-6.

[10] J. H. Kwak, L. Kovarik, and J. Szanyi, "CO_2 reduction on supported Ru/Al2O3 catalysts: cluster size dependence of product selectivity," ACS catalysis, 3 (2013) 2449-2455.

[11] S. S. Kim, H. H. Lee, and S. C. Hong, "A study on the effect of support's reducibility on the reverse water-gas shift reaction over Pt catalysts," Applied Catalysis A: General, 423 (2012) 100-107.

[12] J. A. Loiland, M. J. Wulfers, N. S. Marinkovic, and R. F. J. C. S. Lobo, "Fe/γ-Al_2O_3 and Fe–K/γ-Al_2O_3 as reverse water-gas shift catalysts," Catalysis Science &Technology, 6 (2016) 5267-5279.

[13] A. Zakharova, M. W. Iqbal, E. Madadian, and D. S. Simakov, "Reverse Microemulsion-Synthesized High-Surface-Area Cu/γ-Al_2O_3 Catalyst for CO_2 Conversion via Reverse Water Gas Shift," ACS Applied Materials & Interfaces, 14 (2022) 22082-22094.

[14] F.-m. Sun, C.-f. Yan, C.-q. Guo, and S.-l. Huang, "Ni/Ce–Zr–O catalyst for high CO_2 conversion during reverse water gas shift reaction (RWGS)," International journal of hydrogen energy, 40 (2015) 15985-15993.

[15] B. Bulfin et al., "Analytical model of CeO_2 oxidation and reduction," The Journal of Physical Chemistry C, 117 (2013) 24129-24137.

[16] L. Chen, P. Fleming, V. Morris, J. D. Holmes, and M. A. Morris, "Size-related lattice parameter changes and surface defects in ceria nanocrystals," The Journal of Physical Chemistry C, 114 (2010) 12909-12919.

[17] F. Cao et al., "Influence of oxygen vacancies of CeO_2 on reverse water gas shift reaction," Journal of Catalysis, vol. 414, pp. 25-32, 2022.

[18] B. Dai, S. Cao, H. Xie, G. Zhou, and S. Chen, "Reduction of CO_2 to CO via reverse water-gas shift reaction over CeO_2 catalyst," Korean Journal of Chemical Engineering, 35 (2018) 421-427.

[19] G. Zhou, B. Dai, H. Xie, G. Zhang, K. Xiong, and X. Zheng, "CeCu composite catalyst for CO synthesis by reverse water–gas shift reaction: Effect of Ce/Cu mole ratio," Journal of CO2 Utilization, 21 (2017) 292-301.

[20] T. Zhang, R. Qu, W. Su, and J. Li, "A novel Ce–Ta mixed oxide catalyst for the selective catalytic reduction of NO_x with NH_3," Applied Catalysis B: Environmental, 176 (2015) 338-346.

[21] W. Luhui, S. Zhang, and L. Yuan, "Reverse water gas shift reaction over Co-precipitated Ni-CeO_2 catalysts," Journal of rare earths, 26 (2008) 66-70.

[22] C. Sun, P. Beaunier, V. La Parola, L. F. Liotta, and P. Da Costa, "Ni/CeO_2 nanoparticles promoted by yttrium doping as catalysts for CO_2 methanation," ACS Applied Nano Materials, 3 (2020) 12355-12368.

[23] L. Pastor-Pérez, F. Baibars, E. Le Sache, H. Arellano-Garcia, S. Gu, and T. R. Reina, "CO_2 valorisation via reverse water-gas shift reaction using advanced Cs doped Fe-Cu/Al_2O_3 catalysts," Journal of CO_2 utilization, 21 (2017) 423-428.

[24] Y. Yang, H. Chen, B. Zhao, and X. Bao, "Size control of ZnO nanoparticles via thermal decomposition of zinc acetate coated on organic additives," Journal of crystal growth, 263 (2004) 447-453.

[25] M. Purica, E. Budianu, E. Rusu, M. Danila, and R. Gavrila, "Optical and structural investigation of ZnO thin films prepared by chemical vapor deposition (CVD)," Thin Solid Films, vol. 403, pp. 485-488, 2002.

[26] J.-H. Lee, K.-H. Ko, and B.-O. Park, "Electrical and optical properties of ZnO transparent conducting films by the sol–gel method," Journal of crystal growth, 247 (2003) 119-125.

[27] R. Ayouchi, D. Leinen, F. Martın, M. Gabas, E. Dalchiele, and J. Ramos-Barrado, "Preparation and characterization of transparent ZnO thin films obtained by spray pyrolysis," Thin solid films, 426 (2003) 68-77.

[28] Z.-M. Dang, L.-Z. Fan, S.-J. Zhao, and C.-W. Nan, "Preparation of nanosized ZnO and dielectric properties of composites filled with nanosized ZnO," Materials Science & Engineering: B, 99 (2003) 386-389.

[29] C. Chen, P. Liu, and C. Lu, "Synthesis and characterization of nano-sized ZnO powders by direct precipitation method," Chemical Engineering Journal, 144 (2008) 509-513.

[30] J. Epp, "X-ray diffraction (XRD) techniques for materials characterization," in Materials characterization using nondestructive evaluation (NDE) methods: Elsevier, (2016) 81-124.

[31] B. Greenberg, "Bragg's law with refraction," Acta Crystallographica Section A: Foundations of Crystallography, 45 (1989) 238-241.

[32] A. Patterson, "The Scherrer formula for X-ray particle size determination," Physical review, 56 (1939) 978.

[33] V. Rakić and L. Damjanović, "Temperature-programmed desorption (TPD) methods," Calorimetry and thermal methods in catalysis, (2013) 131-174.

[34] S. L. Schroeder and M. Gottfried, "Temperature-programmed desorption (TPD) thermal desorption spectroscopy (TDS)," Adv. Phys. Chem. Lab, FU Berlin, (2002) 1-22.

[35] A. M. Pollard, Analytical chemistry in archaeology. Cambridge University Press, 2007.

[36] M. Levine, "ICP-Oes–ICP Chemistry, ICP-Oes Analysis, Strengths and Limitations," Technology Networks, 2021.

[37] BET SPECIFIC SURFACE AREA & PORE SIZE ANALYZER, 2024. Available: https://www.microtrac.com/products/gas-adsorption-measurement/surface-area-pore-size-distribution/belsorp-mr-1/

[38] J. Baek, H.-M. Lee, J.-S. Roh, H.-S. Lee, H. S. Kang, and B.-J. Kim, "Studies on preparation and applications of polymeric precursor-based activated hard carbons: I. Activation mechanism and microstructure analyses," Microporous and Mesoporous Materials, 219 (2016) 258-264.

[39] Y. Zhuang, R. Currie, K. B. McAuley, and D. S. Simakov, "Highly-selective CO_2 conversion via reverse water gas shift reaction over the 0.5 wt% Ru-promoted $Cu/ZnO/Al_2O_3$ catalyst," Applied Catalysis A: General, 575 (2019) 74-86, 2019.